OBSERVATIONS OF FERROELASTIC SWITCHING BY RAMAN

SPECTROSCOPY

A Thesis

by

AMY MARIE BOLON

Submitted to the Office of Graduate Studies of
Texas A&M University
in partial fulfillment of the requirements for the degree of

MASTER OF SCIENCE

December 2011

Major Subject: Mechanical Engineering

Observations of Ferroelastic Switching by Raman Spectroscopy

OBSERVATIONS OF FERROELASTIC SWITCHING BY RAMAN

SPECTROSCOPY

A Thesis

by

AMY MARIE BOLON

Submitted to the Office of Graduate Studies of
Texas A&M University
in partial fulfillment of the requirements for the degree of

MASTER OF SCIENCE

Approved by:

Chair of Committee,   Molly Gentleman
Committee Members,   Raymundo Arroyave
    Miladin Radovic
Head of Department,   Sai Lau

December 2011

Major Subject: Mechanical Engineering

ABSTRACT

Observations of Ferroelastic Switching by Raman Spectroscopy.

(December 2011)

Amy Marie Bolon, B.S., Texas A&M University

Chair of Advisory Committee: Dr. Molly Gentleman

Thermal barrier coatings (TBCs) have become an important part of turbine technology by providing thermal protection to the underlying metallic components. These coatings are typically made from a zirconia-based ceramics which have a low thermal conductivity and thermal expansion coefficients similar to those of the superalloys. Early failure in these coatings is most often due to foreign object damage and erosion resulting in delamination and spallation. To protect against these types of failure, new materials with increased toughness are needed. There are two main toughening mechanisms in ceramics: transformation toughening, which is limited to low temperature applications and ferroelastic toughening which is accessible at all temperatures. Ferroelastic toughening occurs when the c-axis of the tetragonal grain undergoes reorientation under the application of an external stress. In this study, ferroelastic toughening is examined by Raman spectroscopy. It is shown that by using polarized confocal Raman spectroscopy one can not only observed the ferroelastic process, but also measure the parameters that control the increase in toughness observed.

Ferroelastic toughening was observed in two ways in the 18mol% ceria stabilized zirconia (18CSZ) samples studied here. Samples were either exposed to indentation

damage or uniaxial loading. In both of these cases maps of the ceramic surface were taken using Raman spectroscopy following loading and the relative intensities of the tetragonal peaks were analyzed. The resulting intensity profiles were used to monitor the reorientation of domains corresponding to ferroelastic toughening. Changes in domain orientation were observed that corresponded to the reorientation of domains along cracks as well as on a larger scale along those cracks. Domain reorientation was also observed under uniaxial loading and the stresses required for domain formation and movement were measured.

DEDICATION

I dedicate this thesis to my parents, thanks for all your love and support.

ACKNOWLEDGEMENTS

NOMENCLATURE

TGO	Thermally grown oxide
TBC	Thermal barrier coating
YSZ	Yttria stabilized zirconia
18CSZ	18mol% ceria stabilized zirconia
EB-PVD	Electron-beam physical vapor deposition
APS	Air plasma spraying
CMAS	Calcium-magnesium-alumino-silicates
FOD	Foreign object damage
TEM	Transmission electron microscopy
TOM	Transmission optical microscopy

TABLE OF CONTENTS

LIST OF FIGURES

LIST OF TABLES

CHAPTER I

INTRODUCTION AND LITERATURE REVIEW

Thermal Barrier Coatings

Turbine engines have gone through many improvements over the last several decades due to improved design, combustion, and materials that have led to an increase in the maximum operating temperature[1-5]. Although increasing operating temperatures improves the efficiency of the turbine engine by reducing fuel consumption and emissions[1, 6], it also threatens the structural integrity to the turbine blades, which generally have melting temperatures in the range of $950°C$[6]. In order to operate at higher temperatures, industry has moved towards the use of multilayer coating systems to decrease the heat load on the metallic components[2-3, 7-8]. The design of the thermal barrier systems has been identified as the limiting factor in the durability and maximum operating temperature of turbines engines making the development of new materials essential in the future of thermal barrier coating and engine performance[7, 9]. These systems, Figure 1, are composed of four parts: (1) a nickel or cobalt-based superalloy substrate[10], (2) an aluminum based bond-coat layer[9], (3) a thermally grown oxide layer that forms *in situ* on the bond-coat[11], and (4) the thermal barrier layer consisting of a low thermal conductivity ceramic and referred to as a thermal barrier coating (TBC)[1-3, 6]. This system works by creating a thermal gradient across the ceramic topcoat and the underlying air-cooled metallic superalloy. The ceramic commonly used for TBCs are

_____

This thesis follows the style of *Journal of American Ceramic Society*.

chosen for their low thermal conductivity and can result in temperature drops across the thickness of the coating of up to 300°C in ~200μm[1, 8, 12-13]. Because of the stringent requirements of operating at higher temperatures, understanding the mechanisms and failure conditions of TBC has become a main driving factor in the design of TBC systems. In particular, "prime reliance," or designing the safe performance criteria so the TBC does not fail during use based on the type of coating and the type of engine, is the primary goal of the next generation of TBCs[14]. As a result, a significant amount of effort is being put into designing higher toughness materials, which have the potential to minimize failure due to impact and erosion damage[7, 9, 15-16].
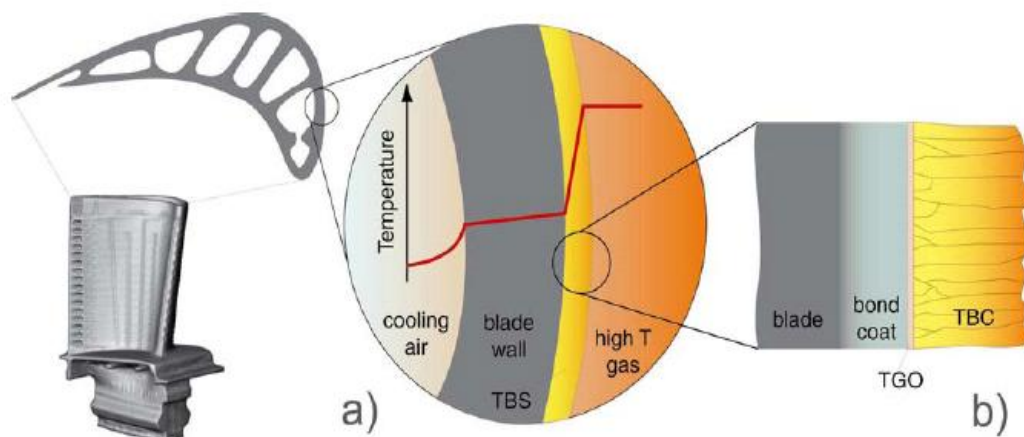
Figure 1. The thermal barrier system on a turbine blade. a) Shows the temperature distribution across the system (red line) going from the high temperature gas to the cooling air. The large temperature drop across the coating allows the system to operate at higher temperatures. b) A breakdown of the thermal barrier system showing the metallic blade, the bond coat, the thin TGO and the columnar TBC.

The requirements for thermal barrier materials include (1) high melting temperature above the operating temperature of the turbine, (2) low thermal conductivity, (3) high coefficient of thermal expansion that is similar to the metallic substrate, (4) thermal and chemical stability, (5) phase stability during thermal cycling, and (6) low sintering activity[15, 17-20]. Operation at high temperatures requires a low thermal conductivity material to decrease the temperature the metallic substrate experiences. An example of the temperature profile seen in these systems is illustrated in Figure 1a. In order to prevent large strains within the thermal barrier system on thermal cycling, the TBC needs to have a coefficient of thermal expansion that is similar to the metallic substrate, which is approximately 10×10^{-6} K^{-1} [2, 9, 15, 21]. A comparison of possible thermal barrier materials is shown in Figure 2 based on the thermal conductivity and the thermal expansion coefficient. This figure shows that zirconia based ceramics have the best combination of low thermal conductivities and high coefficients of thermal expansion making them particularly good candidate materials for TBCs.[3]. In addition to strain requirements of the TBC material, the sintering behavior of the material has a significant impact on the strain compliance of the coating. Sintering in these materials results in loss of strain compliance of the materials as well as a decrease the porosity that concomitantly increases the thermal conductivity of the coating[15, 20]. The choice of materials with poor sinterability results in high levels of porosity that lower the thermal conductivity of the coating and increases the thermal shock resistance which can increase the lifetime of the coating[6, 8-9, 13, 19-20, 22].
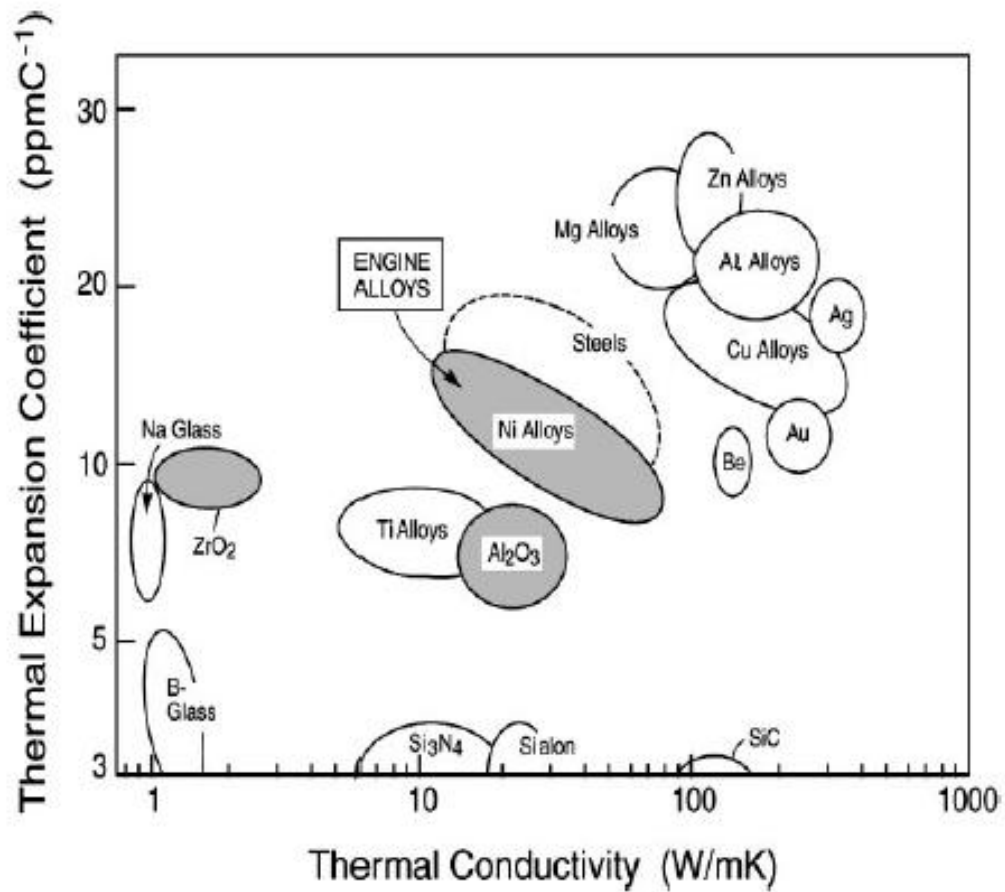
Figure 2. A comparison of different materials based on their thermal conductivity and thermal expansion coefficient for use in a thermal barrier system[3].

Current state of the art TBCs are made of either metastable 7-8 wt% yttria stabilized zirconia (YSZ) or rare earth metal zirconates[7, 9, 12-13, 20]. YSZ was first chosen as a TBC material because of its relatively low thermal conductivity and large coefficient of thermal expansion[7, 15, 23-25]. Unfortunately, as turbine operating temperatures continue to increase, the metastsability of the YSZ system threatens the structural integrity of the coating. At elevated temperatures, YSZ decomposes from the metastable t' phase into the equilibrium yttria-rich cubic and yttria-poor tetragonal phases, seen in the phase diagram in Figure 3[24]. This is a problem because the equilibrium yttria-poor phase undergoes a phase transformation to monoclinic upon cooling that results in a 4% volume expansion capable of inducing significant damage to the coating. Additionally porous YSZ coatings sinter at an accelerated rate at increased turbine temperatures dramatically reducing their strain compliance by increasing the elastic modulus and reducing their thermal shock resistance and increasing the thermal conductivity[3].
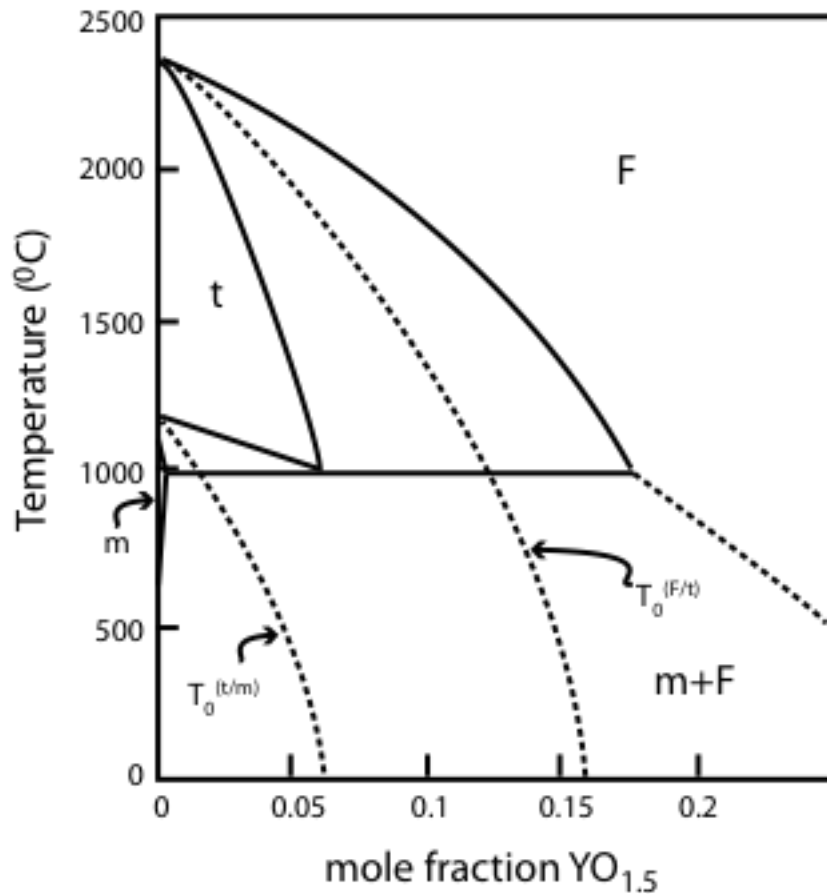
Figure 3. The phase diagram for low mole fractions of $YO_{1.5}$-ZrO_2 shows that at low mole fractions of $YO_{1.5}$ it is easy to suppress the monoclinic phase and form the tetragonal phase. However, at higher concentrations of $YO_{1.5}$ it forms the cubic phase[26].

Gadolinium zirconate, another commonly used thermal barrier material, has several benefits of 7-8YSZ. For example, it has a lower thermal conductivity than YSZ, excellent phase stability at high temperatures, is resistant to molten salt attack, and is resistant to sintering while maintaining a similar coefficient of thermal expansion. However, rare earth zirconates are not in thermodynamic equilibrium with the TGO so they require the use of a buffer YSZ layer[7, 12-13, 20]. The phase diagram for the $GdO_{1.5}$-

ZrO_2-$AlO_{1.5}$ system at 1250°C is shown in Figure 4, the composition $Gd_2Zr_2O_7$ is marked. This composition has a pyrochlore structure, when alumina is introduced to that structure it becomes the perovskite gadolinium aluminate (GAP) phase with a different thermal expansion coefficient[27]. Additionally, gadolinium zirconate has very poor toughness due to its cubic structure that precludes both transfomation toughening and ferroelastic toughening.
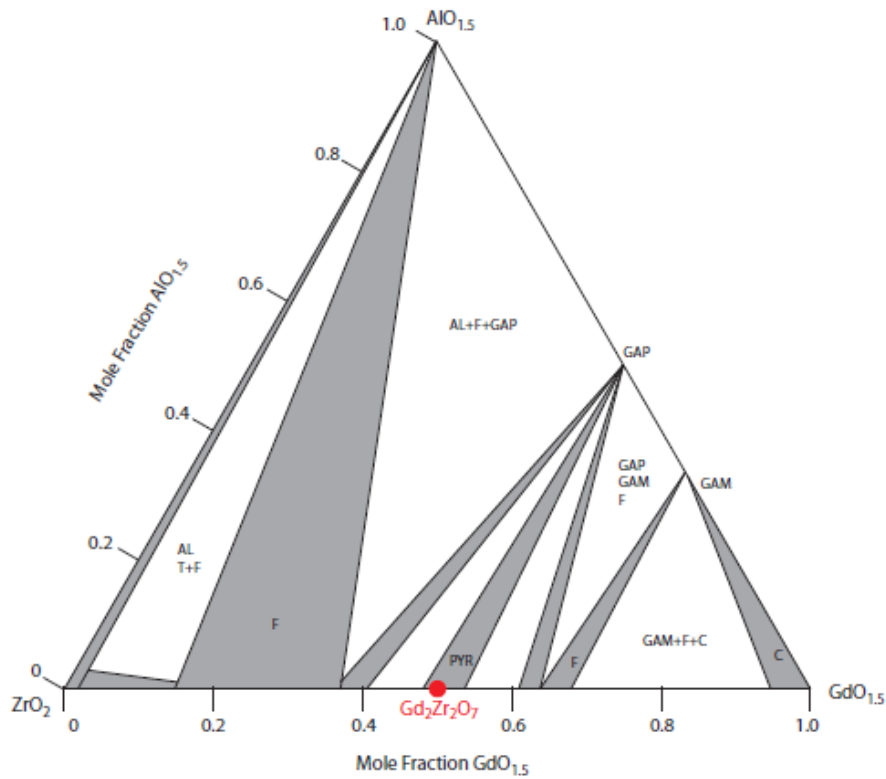
Figure 4. The figure shows the phase diagram for the $GdO_{1.5}$-ZrO_2-$AlO_{1.5}$ system. The composition $Gd_2Zr_2O_7$ is not thermodynamically stable with the TGO, a phase change to a perovskite structure occurs when the pyrochlore phase comes in contact with alumina[27].

The advantages, disadvantages and properties of these materials as well as 18mol% ceria stabilized (18CSZ) (the materials used for the studies described here) are summarized in Table 1.

Table 1. The table gives a summary of the advantages and disadvantages of thermal barrier materials and their properties[12-13, 15, 18, 23, 28-32].

	Advantages	Disadvantages	Properties
7YSZ	High thermal expansion coefficient Low thermal conductivity High thermal shock resistance High toughness	Poor sintering resistance Metastable Poor resistnace to motlen salt attack	$\alpha=10.7 \times 10^{-6}\,K^{-1}$ $k=2.3 Wm^{-1}K^{-1}$ $c/a=1.013$
$Gd_2Zr_2O_7$	High thermal expansion coefficient Low thermal conductivity Phase stable Highly sintering resistant	Not phase compatible with TGO Poor toughness	$\alpha=11 \times 10^{-6}\,K^{-1}$ $k=1.3 Wm^{-1}K^{-1}$
18CSZ	High thermal expansion coefficient Low thermal conductivity Corrosion resistant High toughness	CeO_2 low vapor pressure Poor sintering resistance	$\alpha=10.5\text{-}12 \times 10^{-6}\,K^{-1}$ $k=0.5\text{-}1 Wm^{-1}K^{-1}$ $c/a=1.017$

TBCs are most commonly fabricated using electron-beam physical vapor deposition (EB-PVD) and air plasma spraying (APS)[3, 7, 33-34]. EB-PVD is generally reserved for aerospace-based turbine blades because it provides thickness and surface roughness control but is time and cost intensive. APS on the other hand, is used for energy blade applications and combustor liners where thickness and surface roughness requirements are not as stringent[3, 6, 22]. EB-PVD coatings typically have higher thermal conductivities, higher strain tolerance, lower surface roughness, and erosion rate compared to APS coatings, all properties for 7YSZ are summarized in Table 2[35]. The coatings fabricated by EB-PVD are characterized by large single crystal columnar

structures with intra and inter-columnar porosity that decrease the thermal conductivity of the coating because there is more surface area to the coating than a dense sample[22, 35]. The coatings fabricated by plasma spraying have intersplat porosity with induced vertical cracks[8, 36]. The cracks parallel to the surface occur from poor contact during spraying, these cracks are critical to reducing the thermal conductivity of the coating; the vertical cracks occur due to microcracking during cooling[35]. These columnar structures are formed to improve the strain compliance between the ceramic coating and metallic substrate[1, 16, 22, 35-37]. Example microstructures of both of these coating morphologies as taken from the literature are seen in Figure 5. The thermal and mechanical properties vary widely depending on the type of deposition method used[35, 38-41].

Table 2. The table gives summary of the thermal and mechanical properties of EB-PVD and APS 7YSZ coatings[35].

	EB-PVD	APS
Thermal Conductivity	1.5-1.9 $Wm^{-1}K^{-1}$	0.8-1.1 $Wm^{-1}K^{-1}$
Surface Roughness	1 μm	10 μm
Adhesive Strength	400 MPa	20-40 MPa
Erosion rate (normalized)	1	7
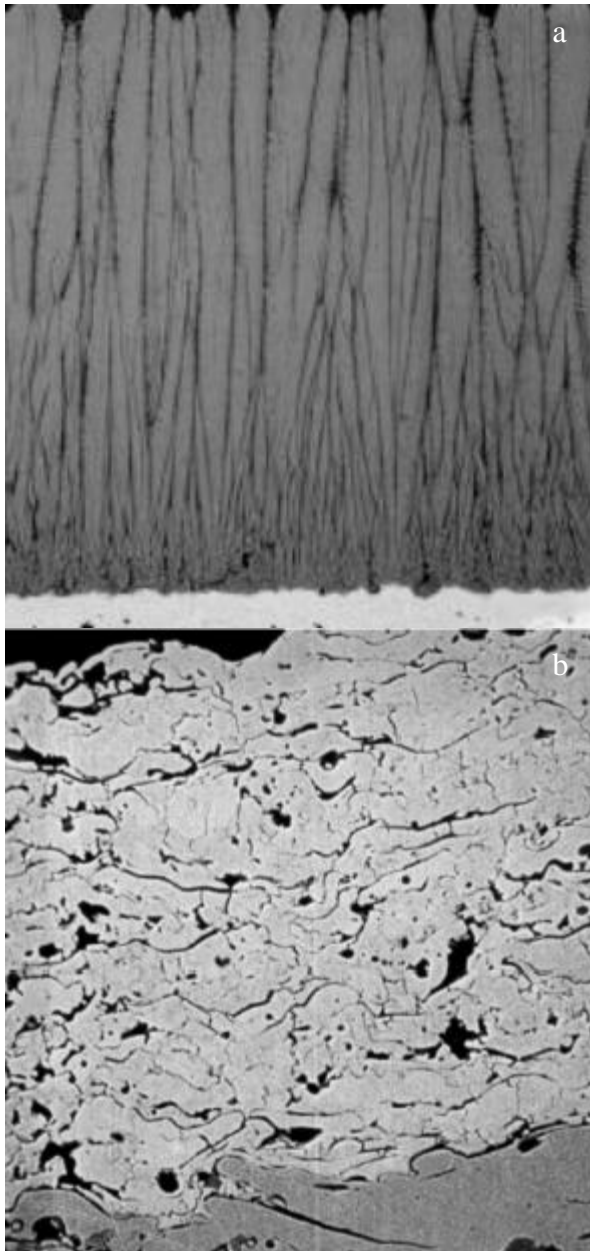
Figure 5. Examples of the microstructures of (a) EB-PVD, with the columnar structure and (b) APS coatings, with intersplat porosity[35].

The most common forms of failure observed in thermal barrier coatings are spallation and buckling during cooling resulting from excessive growth of the thermally

grown oxide layer[3-6], calcium-magnesium-alumino-silicate (CMAS) deposition and solidification[42-43], and erosion and foreign object damage[44]. TGO growth, Figure 6, is currently being addressed by changes in bond-coat composition with an aim to reduce the rate of growth of the alumina scale at elevated temperatures. CMAS deposits on the other hand are airborne contaminates that are typically found in environments with sand or volcanic ash and have a direct impact on the thermal barrier material itself[38]. CMAS deposited on the TBC surface melts at approximately 1150°C and then penetrates into the columnar structure of the coating as shown in Figure 7. Upon cooling, it solidifies increasing the elastic modulus and decreasing porosity of the coating eventually leading to thermal cyclic failure[22, 38, 42-43]. Damage introduced by erosion by micron sized particles and foreign object damage (FOD) has been more difficult to address and potentially more dangerous than oxidation and CMAS because the risk of often infant mortality of the coating[35, 44]. In this failure mechanism, particle impacts cause cracks that propagate through the TBC to the TGO interface causing delamination as illustrated in Figure 8[44]. The extent of the damage observed in the TBC is believed to be related to the toughness of the coating materials. Therefore, the focus of this research is to examine the toughness of candidate thermal barrier materials quickly, thus characterizing their effectiveness at elevated temperatures. To accomplish this goal the toughening mechanism must be identified and a method for measuring the effectiveness of that technique must be developed.
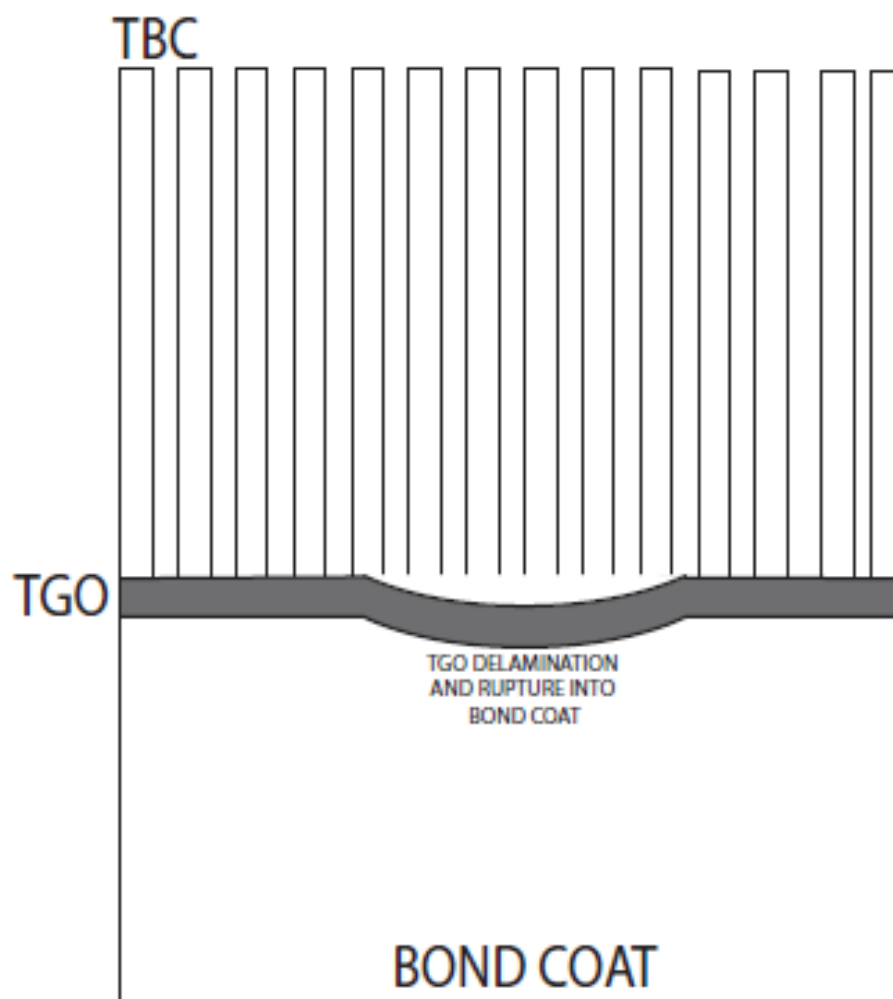
Figure 6. The growth of the TGO eventual results in delamination between the TGO and the TBC, which then results in TGO rupture into the bond coat[22].
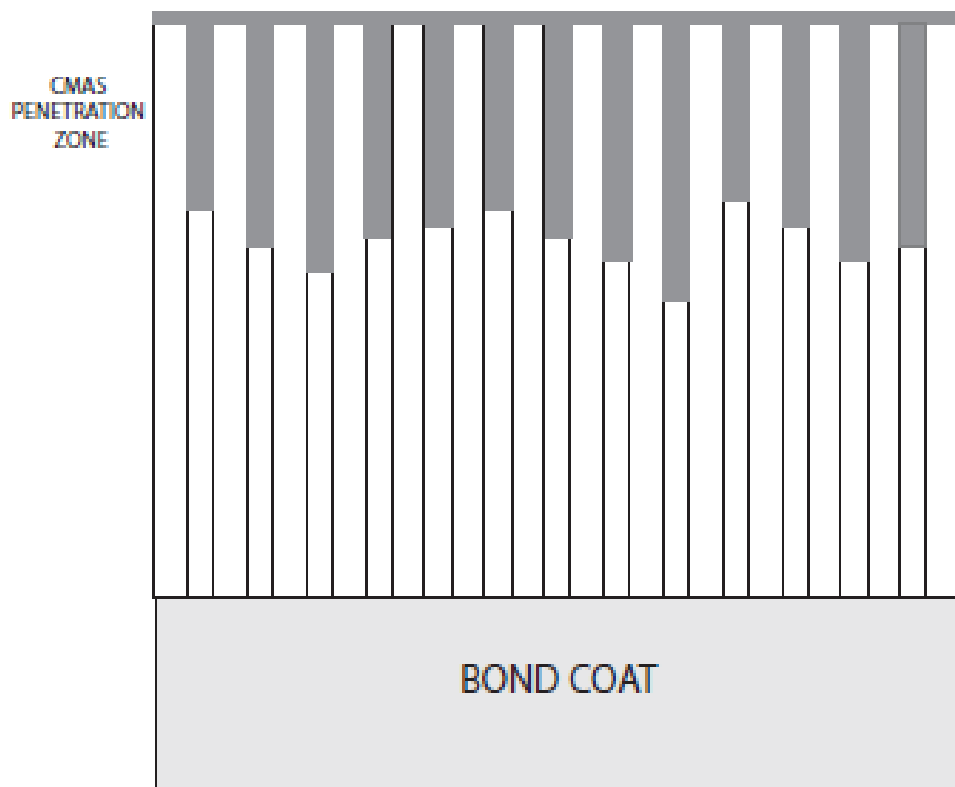
Figure 7. CMAS melts into the columnar structure of the TBC during operation. During cooling, the CMAS hardens and changes the properties of the TBC causing cracking and delamination[22, 42-43].
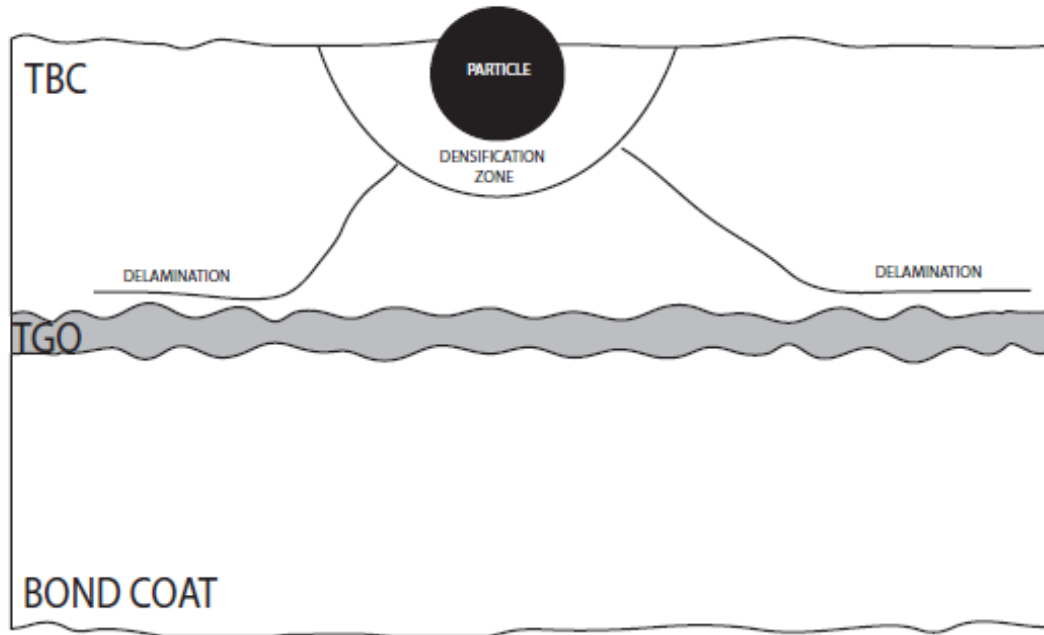
Figure 8. Micron sized particles impact the coating at various angles and velocities causing cracks that can propagate through the TBC eventually causing delamination between the TBC and TGO[44].

Toughening Mechanisms in Ceramics

In ceramic materials there are two major toughening mechanisms: transformation toughening and ferroelastic toughening[29, 45-69]. In transformation toughening a material is fabricated at high temperatures to suppress the equilibrium phase transformation upon cooling resulting in a metastable toughening phase[48, 51, 54, 56, 65, 70]. When a crack tip passes through this material, the metastable phase undergoes a stress induced polymorphic transformation around a crack that results in a compressive stress that acts to close the crack tip as illustrated in Figure 9[48, 54, 70]. In transformation toughened zirconia this transformation occurs from the high temperature tetragonal phase to the

equilibrium monoclinic phase[47-48, 65]. In YSZ transformation toughened ceramics there is a large volume change associated with this transformation (4 percent)[71]. For the crack to propagate following closure by transformation toughening it will have to overcome the compressive stress provided by the phase transformation in addition to the characteristic load for crack propagation[71-72]. Because this toughening mechanism is dependent on a phase transformation it is only available at temperatures below the transformation temperature. In the case zirconia-based systems, this takes place at temperatures below 900°C making it unsuitable for use in thermal barrier systems[53].
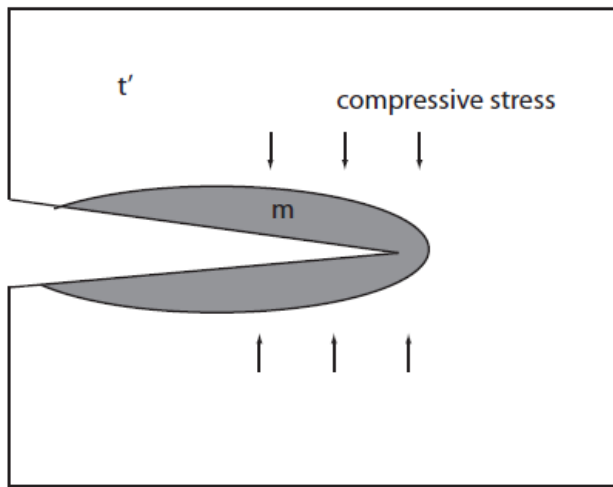
Figure 9. Transformation toughening works in zirconia based materials at low temperatures because there is a 4 percent volume increase associated with the transformation from tetragonal to monoclinic. This volume increase creates compressive stresses that close the crack and make it harder to propagate it further[71-72].

Ferroelastic toughening, on the other hand, has been identified as a mechanism for increasing the toughness of partially stabilized tetragonal zirconia materials at both room and elevated temperatures[46, 52, 68-69, 73]. In ferroelastic toughening the energy absorption process takes place during the local reorientation of the tetragonal domains ahead of the crack tip[45, 50, 52, 66, 68-69]. To be classified as ferroelastic, a material must possess at least two energetically equivalent states and must be able to switch between those states under an applied load[50, 52, 68-69]. Ferroelasticity is the mechanical analog of ferroelectricity and ferromagnetism where instead of electric or magnetic field causing a spontaneous strain, an applied mechanical stress results in a spontaneous strain in the material[45, 63]. The coercive stress is the stress required for domain switching in a material and must be overcome for ferroelastic toughening to be effective [45-46, 50, 63, 68-69]. Baither et al., studied the stress-strain relationship in ferroelastic materials, Figure 10, during domain propagation at the coercive stress, there is no increase in stress until all the possible domains switch[46].
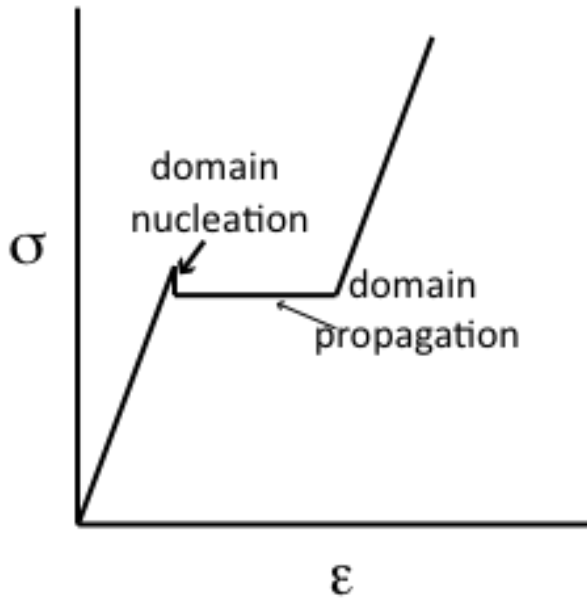
Figure 10. Stress vs strain curve for ferroelastic materials, where there is constant stress during ferroelastic deformation at the coercive stress[46].

In tetragonal zirconias commonly used for thermal barrier coatings, the tetragonality, or c/a ratio, is slightly greater than one and there are three possible equivalent domain orientations with the c-axis in the x, y, or z-directions that are separated by 90° {110} type twin boundaries[46, 49, 52, 72-73]. These domains exist randomly and in equal amounts throughout an as fabricated polycrystalline material[45-46, 50, 52, 63, 68-69, 74]. Upon loading a ferroelastic tetragonal material in the z-direction domains with their c-axis parallel to the z-direction will twin resulting in a 45° reorientation away from the direction of loading, illustrated in Figure 11[49-50, 52, 68-69, 74]. The increase in toughness due to ferroelastic toughening is related to the coercive stress, σ^T, coercive strain, and size of the process zone as described in Equation 1[75]. Here f is the volume

fraction of the material in the process zone, h is the width of the process zone and ε^T is the ferroelastic strain described by Equation 2[75].

$$\Delta\Gamma_{ss} = 2f\sigma^T\varepsilon^T h \tag{1}$$

$$\varepsilon^T = 2/3(c/a - 1) \tag{2}$$
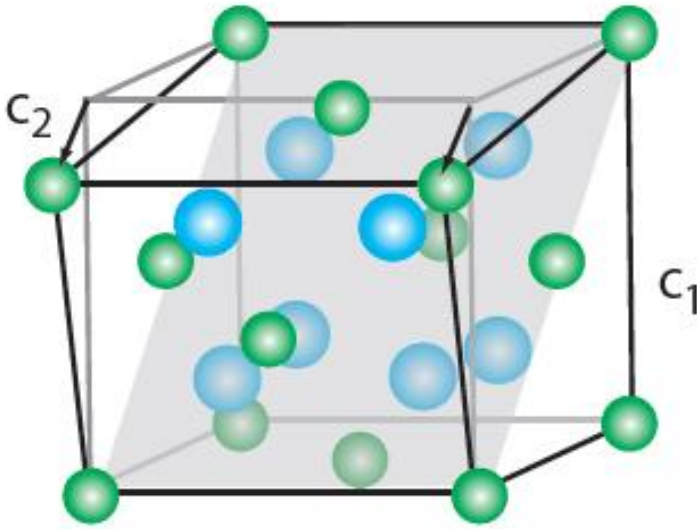
Figure 11. This shows an illustration of the twinning phenomenon that occurs during ferroelastic toughening. The c-axis reorients by 45° away from the direction of loading[76].

To take advantage of this process, studies have been completed in an effort to increase the toughness of ceramics by increasing their tetragonality over standard 7-8 wt% YSZ. This has been done through the addition of tantla and titania to the yttria stabilized systems, Figure 12[29, 67, 77-78]. While the addition of tantalum oxide improved the phase stability up to 1500°C through the formation of a nontransformable tetragonal

phase it does not show a significant increase in toughness regardless of its greatly increased tetragonality[29]. The addition of titanium oxide also exhibited improved phase stability and corrosion resistance, but in this case increased toughness was observed[67]. Although Schaedler and Levi had success with the titanium-yttrium co-doped oxide it is unclear as to the source of the observed improvements and efforts to implement this material in industrial type environment have all failed. To understand these and other results, more research needs to be done to determine the whether this toughening mechanism in active in these material systems[29, 67, 77-78].
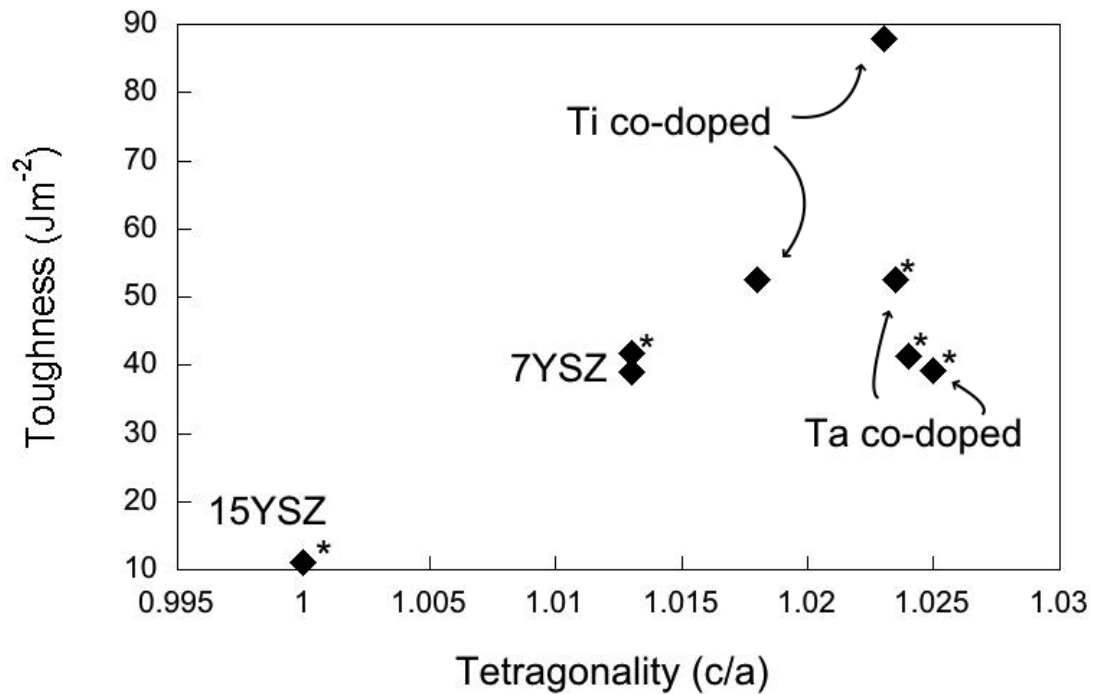
Figure 12. A graph of the toughness versus tetragonality of different tetragonal materials used to begin understanding ferroelastic toughening mechanisms in materials[29, 77].

Raman Spectroscopy

Traditional methods used to observe ferroelastic switching are transmission electron microscopy (TEM), transmission optical microscopy (TOM) and x-ray diffraction[46, 79-80]. In this research a new method to study this phenomenon is described that will overcome the limitations of previously used techniques by eliminating the need for require large single crystals or large grain polycrystalline materials. Raman spectroscopy is an optical microscopy technique that is sensitive to the orientation and crystal structure of materials[81-85]. Raman spectroscopy is based on the inelastic scattering of photons in a material, where there is simultaneous annihilation of the incident photon and creation of the scattered photon[81, 85]. In Stokes Raman scattering, the frequency of the incident phonon is higher than the frequency of the scattered phonon. In this case energy is lost to the system. If the opposite is true, energy is gained from the system, it is an anti-Stokes Raman scattering process[85]. Rayleigh, Stokes and antiStokes scattering energies are illustared in Figure 13. Since Stokes peaks are stronger than anti-Stokes peaks, it is common to only look at the Stokes Raman spectra. This compares to Rayleigh scattering, where the incident and scattered phonon are the same frequency[81]. When looking at a Raman spectrum, the Rayleigh scattering occurs at 0 cm^{-1}, and the peaks for stokes scattering are at different wavelengths depending on the amount of energy lost[81]. A band gap is required for Raman scattering, therefore conductors are not Raman active[86].
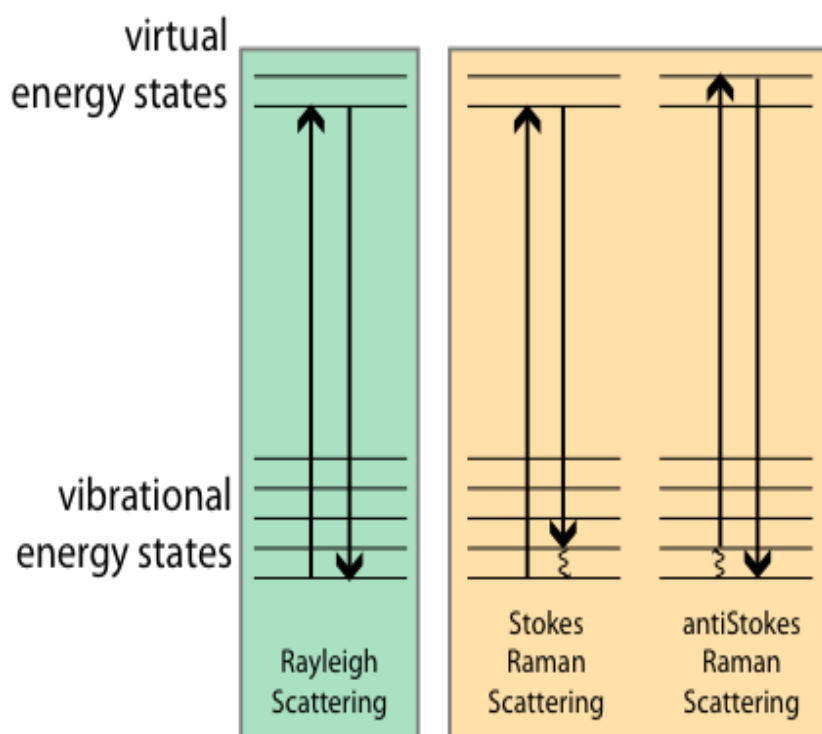
Figure 13. An illustration of the three types of scattering related to Raman spectroscopy. Rayleigh scattering is an elastic scattering process where the energy levels remain the same. Stokes and anti-stokes Raman scattering an inelastic techniques, where the energy lost or gained gives information on the crystal structure of the material[81, 85].

In order for Raman to be a useful tool for characterization of a material, the material must be Raman active, which occurs if the polarizability changes during the activation of a vibrational mode. This change can be caused by a change in the size, shape or orientation of the atoms in the crystal structure. Therefore, Raman can be used to determine the crystal structure and orientation[81]. Raman can also be used to measure the strain present at the atomic level by observing frequency shifts of the Raman peaks resulting from the distorted lattice[87]. In other terms, the vibrational frequencies observed in Raman spectroscopy are proportional to the interatomic forces between the atoms

involved in the vibration. As the material is strained the interatomic forces increase changing the vibrational frequency[86]. In addition, the widths of the Raman peaks correspond to the disorder of the crystal structure, where wider peaks correspond to more disorder on the lattice giving a wider distribution of the average nearest neighbor relationships[82-83, 88].

Polarized Raman spectroscopy, which uses a polarized laser and collection optics, can be used to determine not only the vibration modes but also the orientation crystal being interrogated[81, 86, 89-90]. Raman modes are only active if one of the polarizability components change during irradiation by the laser[81]. A schematic of Porto notation, the notation used to describe the allowed orientation combinations, is given in Figure 14. The incident laser light direction is always given first, the polarization direction of the laser and scattered light are given in parenthesis and the direction of the collected Raman scattered light is the last direction given[81, 89]. Specific Raman peaks can be monitored to observe changes in orientation of the sample using this technique[86]. As a result, if maps of the relative intensities of different modes that are active with different orientations of the c-axis are developed, it is possible to identify regions of ferroelastic toughening where there are changes in orientation of the material at or around damage.
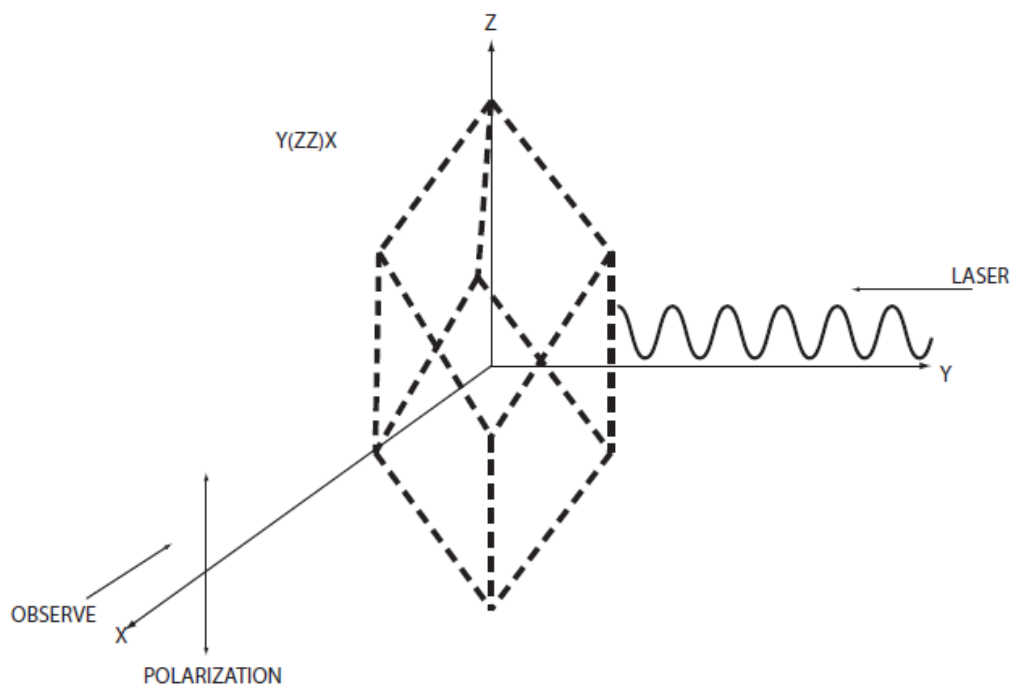
Figure 14. Polarized Raman spectra can be used to determine the crystal orientation of a material. In this figure, the laser light is coming from the y-direction, the polarization occurs in the z-direction and the observer is in the x-direction. The porto notation for this set up is y(zz)-x, this is the standard way of noting the polarization orientation[81, 89].

A typical Raman spectrum for tetragonal ceria stabilized zirconia is seen in Figure 15 and is consistent with the mode identification for yttria-stabilized zirconia[91-92]. When analyzing the Raman maps, the intensities of the tetragonal peaks were tracked as a function of position and load to determine what orientation of the tetragonal crystal. The tetragonal peaks for 18CSZ are the A_{1g} peak at 250cm^{-1} and the B_{1g} peak at 315cm^{-1}. These peaks were chosen because of the relationship between orientation between the crystal and the Raman laser and polarization. The B_{1g} peak is the in-plane c-axis peak,

where the c-axis is perpendicular to the incoming Raman laser. In terms of Porto notation, the B_{1g} peak is maximized for the condition *z(xx)-z*. The A_{1g} mode has the opposite tetragonality meaning. It is the out-of-plane c-axis peak, where the c-axis is parallel to the incoming Raman laser. In Porto notation, the A_{1g} peak is maximized when *x(zz)-x*. To monitor the changing tetragonality, the intensity ratio of the B_{1g} to the A_{1g} peak is monitored. As this intensity ratio decrease, the c-axis tetragonality becomes more and more in-plane[91].
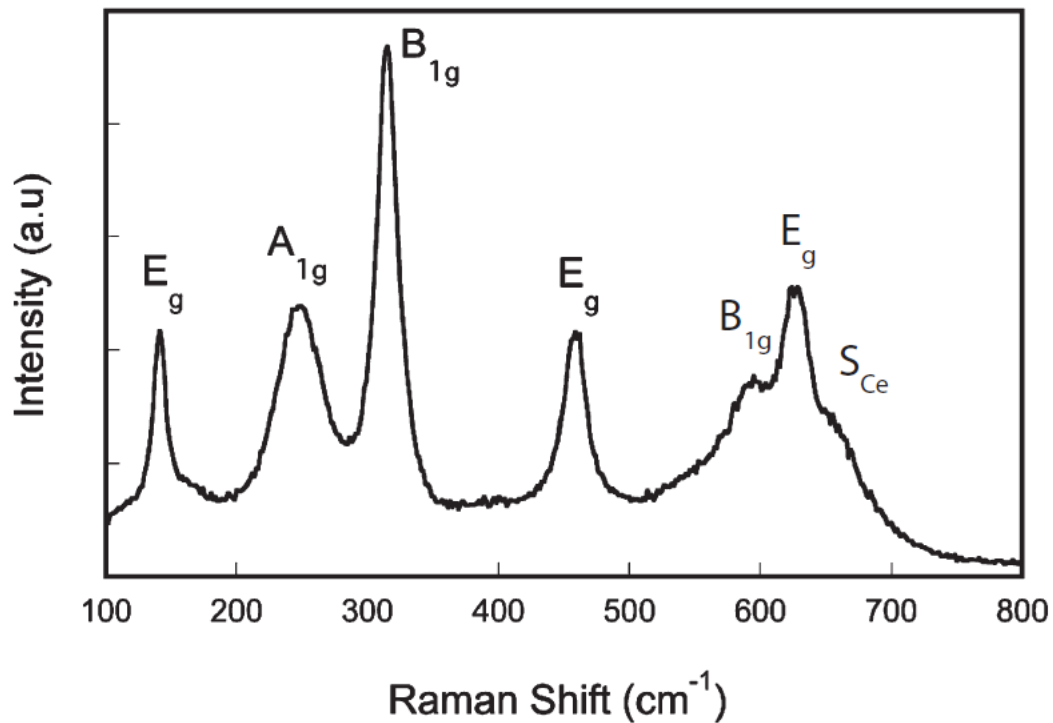
Figure 15. Typical Raman spectra for 18mol% ceria stabilized zirconia showing the presence of typical tetragonal peaks. The monoclinic peaks, approximately 170cm^{-1} and 190cm^{-1} are not observed for this sample.

CHAPTER II

EXPERIMENTAL SETUP

The experimental setup involves the processing the materials to for the sample, the Raman characterization and the data processing.

Material Processing

Because of the benefits listed in the previous section as well as its very low tetragonal to monoclinic transformation temperature, 18 mole percent ceria stabilized zirconia (18CSZ) was chosen for observations of ferroelastic toughening. The powder used to make the ceramic compacts was fabricated using constituent powders of cerium(IV) oxide and zirconium(IV) oxide that were obtained from Alfa Aesar. The cerium(IV) oxide had particle size of 5μm and is 99.9% pure. The zirconium(IV) oxide had a particle size of 5μm and is 99% pure. The equipment used for the processing was a U.S. Stoneware jar mill, a model C Carver lab press, a 1 inch pressing die from MTI Corporation, a Carbolite HTF 18/4 box furnace, polishing paper from Buehler, a Buehler Isoment low speed sectioning saw and a LECO LM300 series Vicker's indent:

1. The constituent powders were combined to make 100 grams of 18CSZ according to the following reaction with 100g of methanol and 150 YSZ grinding media

$$0.18CeO_2 + 0.82ZrO_2 = 23.46gCeO_2 + 76.54gZrO_2 = 18CSZ \tag{1}$$
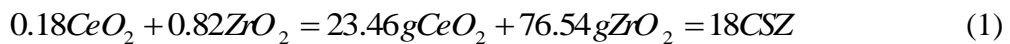
2. The mixture was ball milled at 500 rpm for 24 hours

3. The mixture was drained and the grinding media was filtered out. The remaining liquid was left under a heat lamp overnight until it was dry

4. The dried powder was grinded with a mortar and pestle

5. The grinded powder was then pressed into 1 inch diameter pucks with a thickness of approximately 1/8 inch using the Carver lab press

6. The pucks were placed into alumina crucibles and sintered at 1500°C for 48 hours in the Carbolite box furnace

7. After the pucks were sintered, they were polished to a 0.25µm finish

8. The pucks were divided into two categories. The first group of samples was indented with a Vickers indent. The second group was cut to approximately 1mm cubes with the Isomet sectioning saw

Once the samples were finished, they were analyzed with the Raman system.

Raman Data Collection

The system used to analyze the materials is a Renishaw inVia mapping microRaman spectrometer connected to a Leica microscope equipped with a 532nm line-focus laser. The system is run with Wire 3.2 software. For the samples, data was collected using an 1800 l/mm grating resulting in ~1cm^{-1} resolution and a charge coupled device (CCD) array. In addition a high temperature diamond anvil cell with a 2mm diameter loading surface was used for compression tests within the Raman.

Indent Mapping

The initial Raman studies were done for the indent samples:

1. The system was first calibrated for wavelength and intensity using an internal silicon standard for the 520 cm^{-1} peak

2. The indented samples were taped indent side up onto a glass microscope slide.

3. The glass slide was secured into place on the xyz stage under the microscope

4. The indent was brought into focus under the 50x objective

5. Using the Wire software a map of the indent and the surrounding area was taken with 1 second integration times per spectrum and a 0.3μm step size in the x, and y-directions

6. Following the data analysis, specific regions were identified for depth mapping

7. Using the Wire software, a depth map was done with 1 second integration times per spectrum and a 0.3μm step size in the z-direction

Compression Mapping

The next step in the Raman studies is to look at the effect of a uniaxial stress on the samples. This was done with the compression cell:

1. The 1mm cube samples were loaded into the compression cell on a steel gasket with the polished side up. A piece of sapphire was placed under the sample. A schematic of the loading configuration is shown in Figure 16
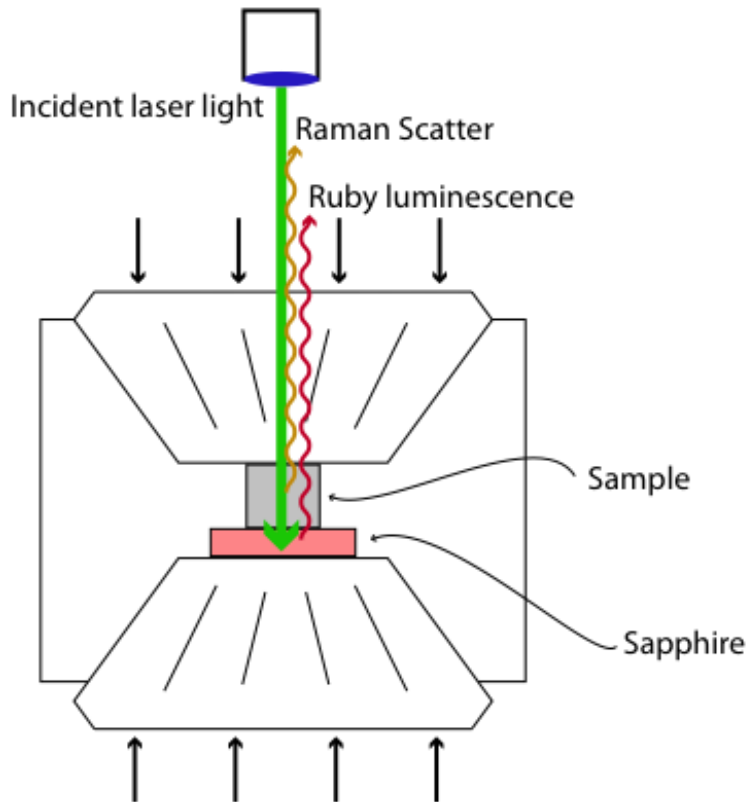
Figure 16. Compression cell setup with the sample and sapphire piece placed between the diamonds. The incident laser light comes in through the top diamond and the returning Raman scatter and ruby luminescence are collected.

2. The compression cell was closed and finger tightened to ensure the sample did

    not move

3. The compression cell was loaded onto the xyz stage in the Raman system

4. Using the long range objective, the surface of the sample was brought into focus

    under the top diamond

5. Using the Wire software, a small map of approximately 3μm by 3μm was taken

    of a selected region using 7 second integration times per spectrum

6. After the map was taken, a 1 second integration time spectrum at 694 wavelengths was taken to measure the ruby luminescence

7. After the data was collected, the screws on the compression cell were tightened ¼ turn and steps 4-6 were repeated at the same spot on the sample

8. This was done for 2 complete turns of the screw, the sample was then unloaded in the same way for 1 complete turn of the screw following steps 4-7

9. After unloading, the sample was loaded again until failure occurred, following steps 4-7

Data Processing

The data collected from the indent mapping and compression mapping was processed using Wire 3.2 software:

1. The data was normalized to an area of 1 along the spectral axis using the integrated signal function within the normalization option of the Wire software

2. The first three peaks were curve fitted using a Gaussian-Lorentzian curve and the fit was saved

3. Under the mapping review analysis option, the intensity of each peak was fitted with the previously made curve fit

4. The intensity of the peak at 320cm^{-1} is divided by the intensity of the peak at 260cm^{-1} using the data arithmetic function

5. The resulting map was adjusted to grey scale with a bicubic interpolation mode to reduce pixelization

To look at the effect of transformation toughening on the materials, the percentage of the monoclinic phase was calculated using the peak areas of the monoclinic (A_m) and tetragonal (A_t) peaks and the following formula[72, 93-94].

$$C_m = \frac{A_m^{170} + A_m^{190}}{0.97\left(A_t^{260} + A_t^{320}\right) + \left(A_m^{170} + A_m^{190}\right)} \tag{2}$$

For the compression testing, the additional ruby luminescence data must be analyzed to determine the load on the samples:

1. The data was normalized to an area of 1 along the spectral axis using the integrated signal function within the normalization option of the Wire software

2. The two luminescence curves were fitted using a Gaussian-Lorentzian curve and the fit was saved

3. The peak position of the right peak was recorded

4. This was repeated for each loading and unloading

5. The load was calculated according to the following equation[95]

$$274\Delta\lambda = P(MPa) \tag{3}$$

CHAPTER III

RESULTS AND DISCUSSION

The monoclinic peaks, which were not seen in any of the 18CSZ samples, Figure 15, would have been at approximately $170cm^{-1}$ and $190cm^{-1}$ this is consistent with no transformation toughening occurring within the material. The monoclinic peaks were seen in titania-yttria co-doped zirconia where transformation toughening occurs. The presence of cubic peaks could not be confirmed in the material because the Raman band for these is too weak and overlaps with the tetragonal bands[96]. The last peak, S_{Ce} is the result of the substitution of Ce onto the Zr sites[96].

Indent Mapping

Several indents were mapped using Raman spectroscopy. The intensities of the B_{1g}/A_{1g} peaks were plotted as a function of position. Figure 17 and Figure 18 show examples of the plotted relative intensities with the white light image of the indent. It can be seen that the grain size away from the indent is approximately 10µm; all mapped samples show a similar grain size. These grains have the same Raman intensity indicating that they are a single domain. Within the indent, there do not appear to be single domain grains, instead, Raman mapping shows intensity contrasts approximately 1µm or less. This is evidence of multiple tetragonal variants in the region due to loading.
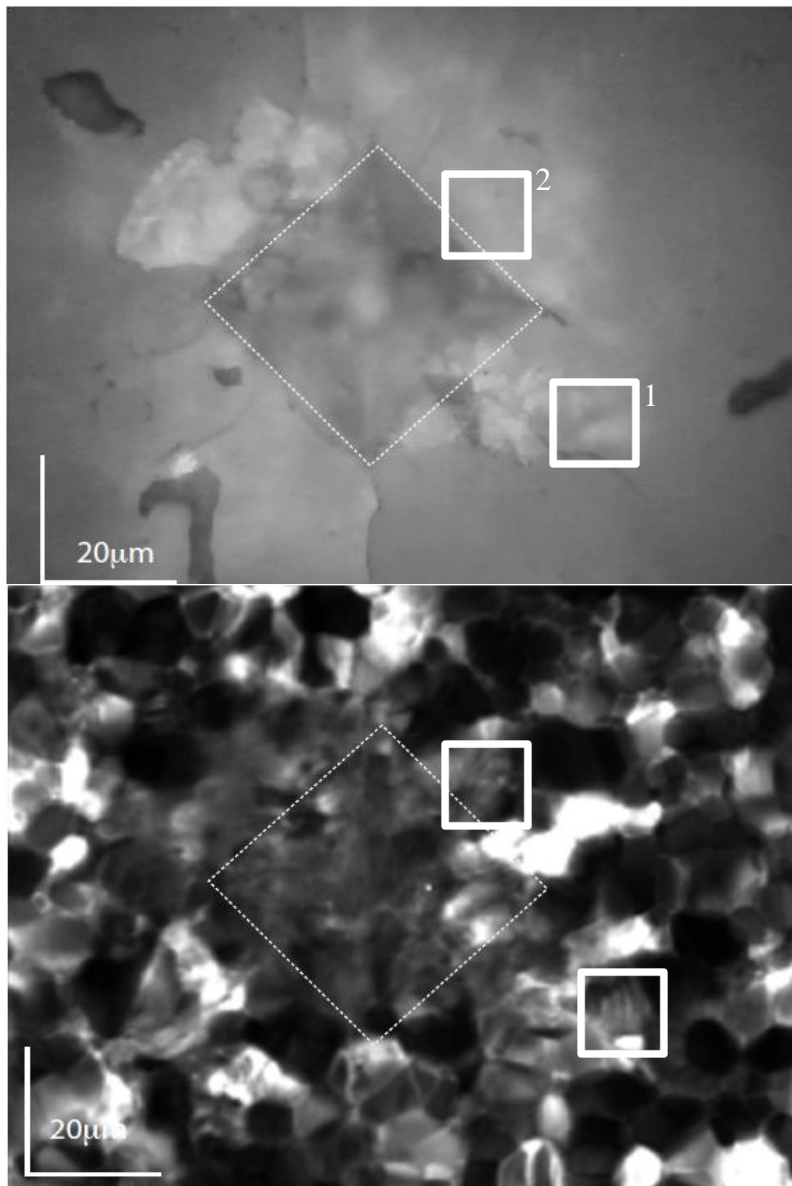
Figure 17. White light and Raman images of an indented region in the bulk material. a) Image of the indent with radial cracks emanating from the corners of the indent. The dashed box highlights the edges of the diamond indent. The solid boxes the location of regions of banding as seen on the Raman map. b) The Raman map of the relative intensities of the B_{1g}/A_{1g} modes for the same region as seen in a. Bright regions indicate that the c-axis is oriented out of the plane of the paper while dark regions indicate that it is oriented in the plane of the paper. The presence of ferroelastic switching in the process zones can be observed by bright areas along the lengths of the cracks as well as the presence of banding in grains near the indents and cracks.
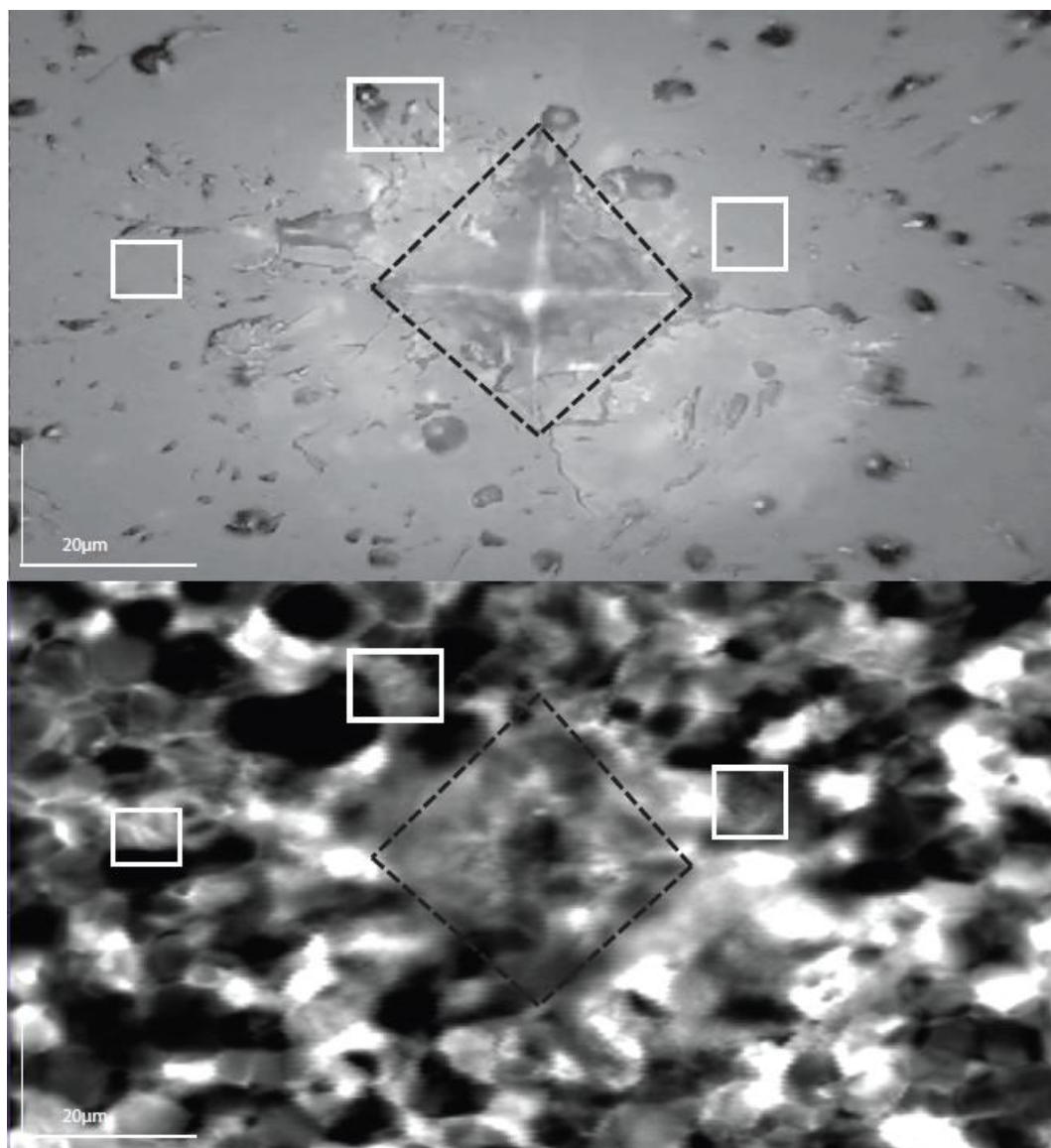
Figure 18. Another white light image and Raman map of an indent in a bulk sample. The banding phenomenon occurs in multiple locations around the indent. It is not currently clear why some grains undergo this banding and some do not.

Ferroelastic Toughening Observations

Additional observations were made around the cracks along the indents. Looking closely at Figure 17, one can see that on the intensity map the cracks appear bright even as they pass through dark grains. The bright region around the cracks is the process zone that develops during loading. During this process, the c-axis shifts from being in-plan to the {110} plane 90° perpendicular to the original plane. The width of the process zone is measured to be approximately 1μm, larger than the spatial resolution of the Raman system which is ~0.7μm.

The highlighted regions in Figure 17 and Figure 18 show grains that exhibit alternating bright and dark Raman intensities. These grains are all approximately 10μm in size and occur near cracks. Figure 19 shows an enlarged image of highlighted region 1 in Figure 17. This image was taken with finer steps than the previous Raman maps. It can be seen that the grain with alternating bands is next to a crack within the material. The alternating bands have a width of slightly more than 1μm and extend across the entire grain. These bands are evidence of the alternating tetragonal orientations due to ferroelastic toughening.
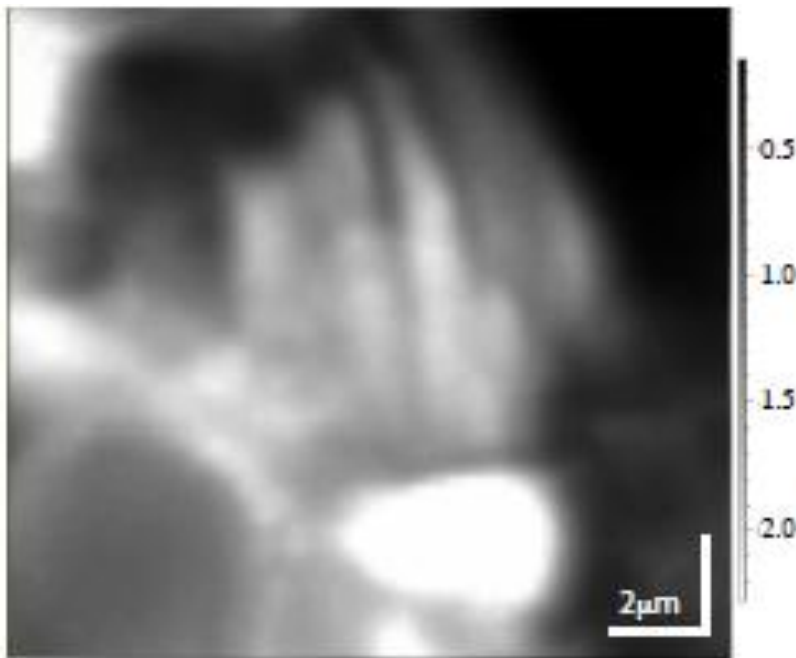
Figure 19. Raman map of a high resolution image of ferroelastic switching. The image clearly illustrates switching along the crack (lower left hand corner) and the presence of ferroelastic domain bands in the bulk of the grain (image center).

A confocal depth slice was taken of the same region with the alternating bands, shown in Figure 20. It can be seen that at depths greater than approximately 5μm there is only one single variant. However, closer to the surface there are alternating light and dark bands showing the ferroelastic toughening is not just a surface phenomenon. The interface between the bulk and the domains formed on the surface is approximately 90°, which is consistent with the {110} type 90° twin boundaries formed from ferroelastic toughening.
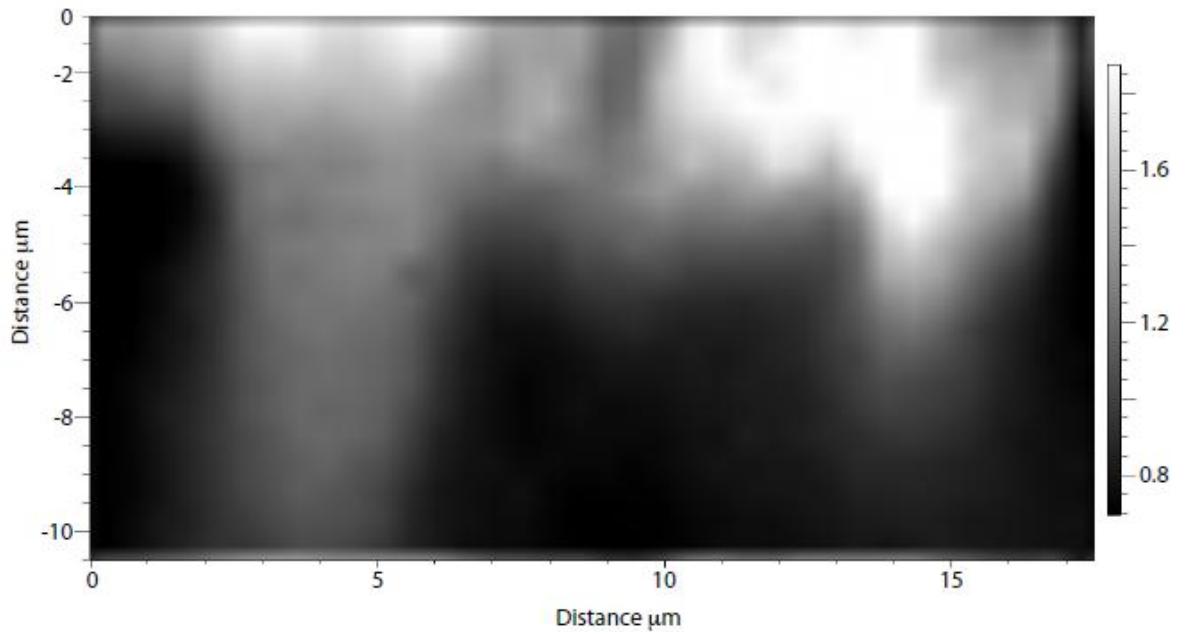
Figure 20. Raman relative intensity map of the B_{1g}/A_{1g} modes for the high-resolution region is seen in Fig. 2(c). Herein, the top of the image corresponds to the surface of the material where ferroelastic domains of c-axis perpendicular to the surface are formed under loading and appear white. Below these domains, the bulk of the grain exhibits single variant in domain with the c-axis within the plane of the surface.

Transformation Toughening Observations

Titania-yttria codoped zirconia samples obtained from University of California Santa Barbara were also indented and studied. The results, Figure 21, show grains that are approximately 5µm, but no clear evidence of ferroelastic switching. Figure 21c shows the percent of the monoclinic phase around an indent. Up to around 20% of the tetragonal phase transformed to the monoclinic phase around the edges of the indent. Areas further away from the indent showed no monoclinic phase present. Since this material can be transformation toughened, ferroelastic switching does not occur.
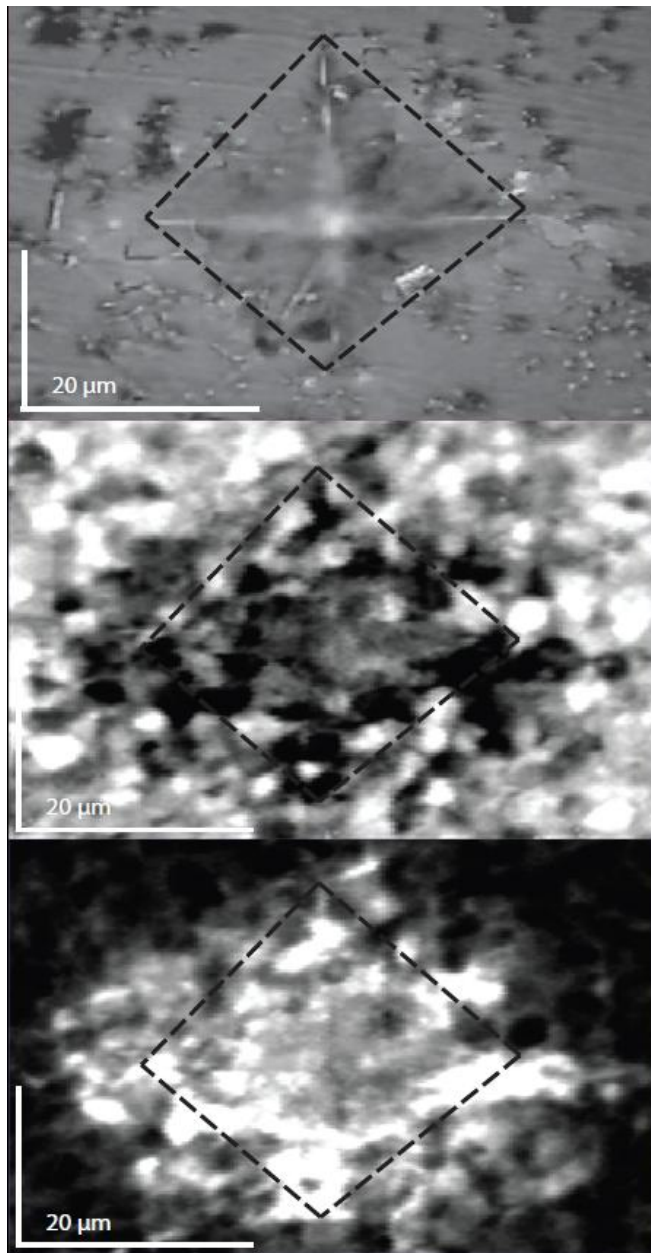
Figure 21. White light, intensity map and percent monoclinic map of an indent on a Titania-yttria codoped zirconia bulk material. a)   There are only a few radial cracks seen extending from the indent. This material is much tougher than 18CSZ. b) The intensity map of the B_{1g}/A_{1g} modes show no evidence of banding indicating ferroelastic toughening and grains approximatly 5μm.   c) Map of the percent monoclinic, the bright areas are approximately 20% monoclinc and the dark areas are no monoclinc. There is more monoclinic around the indent indicating that the main toughening mechanism is transformation toughening and not ferroelastic toughening.

Compression Raman Mapping

Using the diamond anvil cell, Raman maps were taken of sample as a function of load. Again, the relative intensities of the B_{1g}/A_{1g} peaks were calculated to look at the tetragonal orientation. The samples were loaded with a piece of sapphire which produced a ruby R-line luminescence that was used to calculate the load. The relative intensity is plotted against the load in Figure 22. The sample was loaded up to approximately 550MPa, then unloaded to approximately 300MPa and finally loaded again to failure at approximately 800MPa. Upon initial loading, the sample shows a dramatic decrease in the B_{1g}/A_{1g} intensity until approximately 450MPa. Then it shows significant increase upon the next loading to about 550MPa. This is likely due to some kind of failure within the material where the observed grain was unable to provide effective load transfer. Mapped Raman images for this initial loading series are shown in Figure 23. The images show the development and growth of the dark in-plane c-axis as load increases. Figure 23d occurs after the failure event and shows that the dark grain that had been forming is no longer present, which suggests that complete switching of the grain had not yet occurred. Upon unloading and reloading the intensity ratio follows a less severe path. This suggests that the coercive stress was not reached in the material, or domain formation in poorly aligned c-axis grains. When the sample was removed from the diamond anvil cell, it was completely pulverized so additional testing on the sample could not be done. Additional samples were tested and failure events were observed at loads near 550MPa.
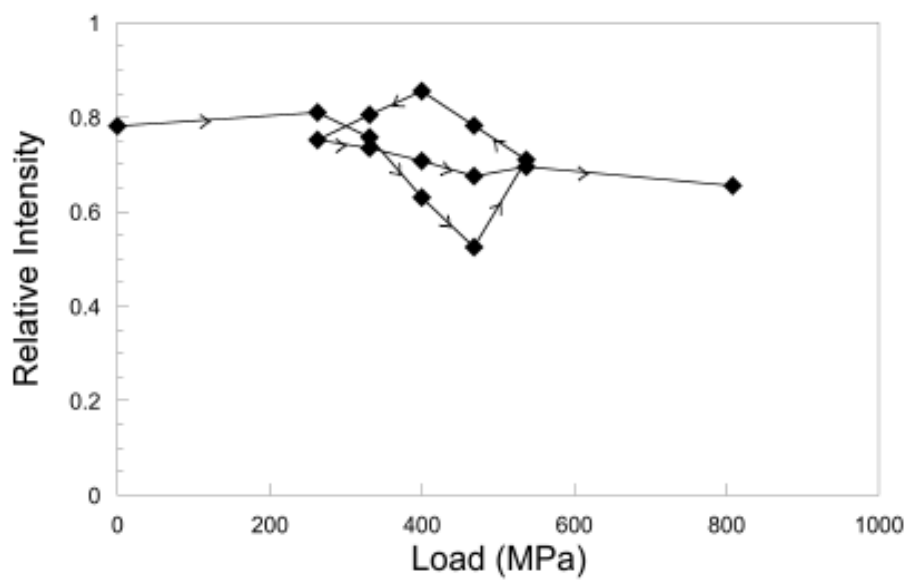
Figure 22. This figure shows the relative intensities of the B_{1g}/A_{1g} modes of 18 mol% ceria-stabilized zirconia as a function of uniaxial loading in the diamond anvil cell. Load measurements were taken using the luminescence of a ruby standard.
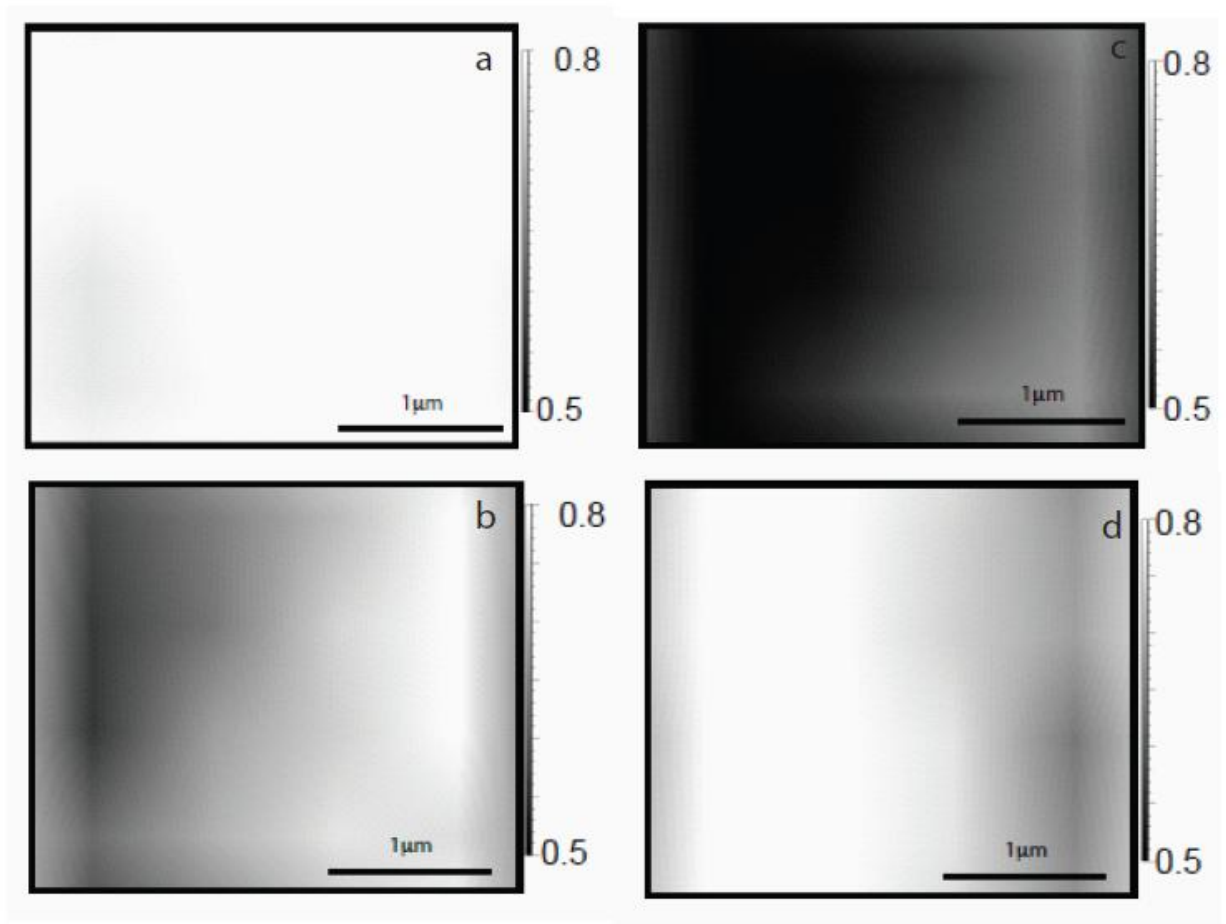
Figure 23. Images of a region of the loaded area taken parallel to the direction of loading. Progressing from a to b to c, the load increases and the percentage of the image that appears dark increases. This is the formation and growth of c-axis in the plane of the page domain. Inset (d) shows the same region after a failure event in the material.

CHAPTER IV

CONCLUSIONS

Ferroelastic switching is an important toughening mechanism for thermal barrier coatings. This phenomenon was studied using Raman spectroscopy by looking at 18 mol% ceria stabilized zirconia. The relative intensity of the tetragonal peaks was monitored as a function of position and load on the surface of the material with respect to induced damage. Mapping of a region around an indent showed large single domain grains far from the indent, but regions of multiple domains in a grain near the indent. The process zone around cracks was measured to be approximately 1μm. Looking closely at grains where ferroelastic domains form show that the domains were approximately 1μm wide and extended the length of the grain, approximately 10μm. The depth profile shows that this is a surface phenomenon, where the newly formed domains only extended approximately 5μm into the grain. The rest of the grain is a single domain. Raman mapping of a different material shows that when transformation toughening occurs, there is no evidence of ferroelastic switching. During uniaxial loading in a diamond anvil, the domain formation and growth was studied as a function of load. The coercive stress of the material was estimated to be approximately 300 MPa based on the results of these tests, while failure typically occurred at approximately 550MPa. These results show that Raman spectroscopy can be use to characterize potential thermal barrier coating materials and observe ferroelastic switching in these materials.

CHAPTER V

FUTURE WORK

The next step in this research is doing neutron diffraction on the 18CSZ samples at various high temperatures to determine the changes in coercive stress as a function of temperature to be directly compared with measurements made by Raman spectroscopy. Diffraction patterns can yield information about the phase of the material, the amount of each phase, and the lattice parameters[49, 97-100]. Neutron diffraction is useful in looking at the crystal structure of the bulk sample because the high penetration of neutrons ensures bulk information, not just surface information that is obtained through Raman scattering[99-101]. Previous work by Ma et al. has been done on 7YSZ, samples were loaded and the relevant tetragonal peaks were monitored for ferroelastic toughening to determine the coercive stress. The results show ferroelastic toughening by looking at the stress-strain curve and a coercive stress of approximately 1.55GPa where the relative intensity of the tetragonal peaks began to change[100]. Cain et al. looked at 14 mol% ceria-stabilized zirconia and found the coercive stress to be 1.02GPa, where the relative intensities of the tetragonal peaks began to change[49]. Howard et al. looked at the changing crystal structure of magnesia-partially-stabilized zirconia using neutron diffraction as a function of temperature. He was able to determine the temperature the majority of the material undergoes a phase transition[98]. These results show that neutron diffraction is a way to determine the coercive stress of a material as a function of temperature and to look at the bulk phase of a material. 18CSZ samples will be analyzed

by looking at the stress-strain curves, the changing relative tetragonal peak intensities and the strains of the tetragonal peaks.

Another phase of this project is to look at the thermal relaxation of the ferroelastic bands as a function of temperature. Samples will be indented with a Vickers indent to cause ferroelastic toughening; those regions will then be mapped *in situ* with a high temperature stage in the Raman system to look at the effect of temperature of the banded regions. There has been a lot of research into thermal effects on piezoelectrics, specifically PZT[102-104] however little research has been done on the effects of temperature on ferroelastic domain motion. Chang et al. studied the thermal effects on tetragonal piezoelectrics and found that the domain walls relax upon heating which reduces the ferroelastic texture. He concluded that the motion of the domain walls is related to the strains within the material during heating and cooling[104]. Initial results show the width of the ferroelastic bands increase at approximately 400°C. This change is similar to what is seen in the piezoelectrics studied by Chang at the Curie temperature[104].

To confirm the results of the neutron diffraction studies, *in situ* compression tests will be conducted at the same temperatures using the diamond anvil cell. Other tests with the diamond anvil cell will include *in situ* indentation with a small diamond to observe the effects of pressure on the ferroelastic bands formation around indents. After final testing with 18CSZ, other stabilized zirconia materials will be fabricated and tested in the same way. Possible stabilizers include ytterbia[76], hafnia and niobia[105].

REFERENCES

[1]M. Belmonte, "Advanced ceramic materials for high temperature applications," *Advanced Engineering Materials,* **8** [8] 693-703 (2006).

[2]A. Bennett, "Properties of thermal barrier coatings," *Materials Science and Technology,* **2** [3] 257-261 (1986).

[3]D. R. Clarke and C. G. Levi, "Materials design for the next generation thermal barrier coatings," *Annual Review of Materials Research,* **33** 383-417 (2003).

[4]B. L. Koff, "Gas turbine technology evolution: A designer's perspective," *Journal of Propulsion and Power,* **20** [4] 577-595 (2004).

[5]C. T. Sims, "Nonmetallic materials for gas-turbine engines - Are they real," *Advanced Materials & Processes,* **139** [6] 32-39 (1991).

[6]P. K. Wright and A. G. Evans, "Mechanisms governing the performance of thermal barrier coatings," *Current Opinion in Solid State & Materials Science,* **4** [3] 255-265 (1999).

[7]C. G. Levi, "Emerging materials and processes for thermal barrier systems," *Current Opinion in Solid State & Materials Science,* **8** [1] 77-91 (2004).

[8]N. P. Padture, M. Gell, and E. H. Jordan, "Materials science - Thermal barrier coatings for gas-turbine engine apptications," *Science,* **296** [5566] 280-284 (2002).

[9]A. G. Evans, D. R. Mumm, J. W. Hutchinson, G. H. Meier, and F. S. Pettit, "Mechanisms controlling the durability of thermal barrier coatings," *Progress in Materials Science,* **46** [5] 505-553 (2001).

[10]C. T. Sims, "Superalloys for advanced energy-systems," *Journal of Metals,* **28** [12] 7-18 (1976).

[11]F. A. Golightly, F. H. Stott, and G. C. Wood, "Influence of yttrium additions on oxide-scale adhesion to an iron-chromium-aluminium alloy," *Oxidation of Metals,* **10** [3] 163-187 (1976).

[12]J. Wu, N. P. Padture, P. G. Klemens, M. Gell, E. Garcia*, et al.*, "Thermal conductivity of ceramics in the ZrO2-GdO1.5 system," *Journal of Materials Research,* **17** [12] 3193-3200 (2002).

[13]J. Wu, X. Z. Wei, N. P. Padture, P. G. Klemens, M. Gell*, et al.*, "Low-thermal-conductivity rare-earth zirconates for potential thermal-barrier-coating

applications," *Journal of the American Ceramic Society,* **85** [12] 3031-3035 (2002).

[14]W. Beele, G. Marijnissen, and A. van Lieshout, "The evolution of thermal barrier coatings - status and upcoming solutions for today's key issues," *Surface & Coatings Technology,* **120** 61-67 (1999).

[15]X. Q. Cao, R. Vassen, and D. Stoever, "Ceramic materials for thermal barrier coatings," *Journal of the European Ceramic Society,* **24** [1] 1-10 (2004).

[16]S. M. Meier and D. K. Gupta, "The evolution of thermal barrier coatings in gas-turbine engine applications," *Journal of Engineering for Gas Turbines and Power-Transactions of the Asme,* **116** [1] 250-257 (1994).

[17]C. H. Liebert and R. A. Miller, "Ceramic thermal barrier coatings," *Industrial & Engineering Chemistry Product Research and Development,* **23** [3] 344-349 (1984).

[18]N. Markocsan, P. Nylen, J. Wigren, and X. H. Li, "Low thermal conductivity coatings for gas turbine applications," *Journal of Thermal Spray Technology,* **16** [4] 498-505 (2007).

[19]R. A. Miller, "Current status of thermal barrier coatings - An overview," *Surface & Coatings Technology,* **30** [1] 1-11 (1987).

[20]R. Vassen, X. Q. Cao, F. Tietz, D. Basu, and D. Stover, "Zirconates as new materials for thermal barrier coatings," *Journal of the American Ceramic Society,* **83** [8] 2023-2028 (2000).

[21]A. G. Evans, D. R. Clarke, and C. G. Levi, "The influence of oxides on the performance of advanced gas turbines," *Journal of the European Ceramic Society,* **28** [7] 1405-1419 (2008).

[22]T. Strangman, D. Raybould, A. Jameel, and W. Baker, "Damage mechanisms, life prediction, and development of EB-PVD thermal barrier coatings for turbine airfoils," *Surface & Coatings Technology,* **202** [4-7] 658-664 (2007).

[23]J. R. Brandon and R. Taylor, "Thermal-properties of ceria and yttria partially stabilized zirconia thermal barrier coatings," *Surface & Coatings Technology,* **39** [1-3] 143-151 (1989).

[24]J. R. Brandon and R. Taylor, "Phase-stability of zirconia-based thermal barrier coatings. 1. Zirconia yttria alloys," *Surface & Coatings Technology,* **46** [1] 75-90 (1991).

[25]P. Duwez, F. H. Brown, and F. Odell, "The zirconia-yttria system," *Journal of the Electrochemical Society,* **98** [9] 356-362 (1951).

[26]O. Fabrichnaya and F. Aldinger, "Assessment of thermodynamic parameters in the system ZrO2-Y2O3-Al2O3," *Zeitschrift Fur Metallkunde,* **95** [1] 27-39 (2004).

[27]S. Lakiza, O. Fabrichnaya, C. Wang, M. Zinkevich, and F. Aldinger, "Phase diagram of the ZrO2-Gd2O3-Al2O3 system," *Journal of the European Ceramic Society,* **26** [3] 233-246 (2006).

[28]R. Taylor, J. R. Brandon, and P. Morrell, "Microstructure, composition and property relationships of plasma-sprayed thermal barrier coatings," *Surface & Coatings Technology,* **50** [2] 141-149 (1992).

[29]F. M. Pitek and C. G. Levi, "Opportunities for TBCs in the ZrO2-YO1.5-TaO2.5 system," *Surface & Coatings Technology,* **201** [12] 6044-6050 (2007).

[30]R. Mevrel, J. C. Laizet, A. Azzopardi, B. Leclercq, M. Poulain*, et al.*, "Thermal diffusivity and conductivity of Zrl-xYxO2-x/2 (x=0, 0.084 and 0.179) single crystals," *Journal of the European Ceramic Society,* **24** [10-11] 3081-3089 (2004).

[31]P. Scardi, R. Dimaggio, L. Lutterotti, and P. Maistrelli, "Thermal-expansion anisotrophy of ceria-stabilized tetragonal zirconia," *Journal of the American Ceramic Society,* **75** [10] 2828-2832 (1992).

[32]J. W. Adams, H. H. Nakamura, R. P. Ingel, and R. W. Rice, "Thermal expansion behavior of single-cyrstal zirconia," *Journal of the American Ceramic Society,* **68** [9] C228-C231 (1985).

[33]J. G. Duh, H. T. Dai, and B. S. Chiou, "Sintering, microstucture, hardness and fracture-toughness behavior of Y2O3-CeO2-ZrO2," *Journal of the American Ceramic Society,* **71** [10] 813-819 (1988).

[34]J. F. Jue and A. V. Virkar, "Fabrication, microstructural characterization, and mechanical-properties of polycrystalline t'-zirconia," *Journal of the American Ceramic Society,* **73** [12] 3650-3657 (1990).

[35]J. R. Nicholls, K. J. Lawson, A. Johnstone, and D. S. Rickerby, "Methods to reduce the thermal conductivity of EB-PVD TBCs," *Surface & Coatings Technology,* **151** 383-391 (2002).

[36]D. Renusch, H. Echsler, and M. Schutze, "Progress in life time modeling of APS-TBC - Part I: residual, thermal and growth stresses including the role of thermal fatigue," *Materials at High Temperatures,* **21** [2] 65-76 (2004).

[37]A. A. Kulkarni, A. Goland, H. Herman, A. J. Allen, J. Ilavsky*, et al.*, "Microstructure-property correlations in industrial thermal barrier coatings," *Journal of the American Ceramic Society,* **87** [7] 1294-1300 (2004).

[38]M. P. Borom, C. A. Johnson, and L. A. Peluso, "Role of environmental deposits and operating surface temperature in spallation of air plasma sprayed thermal barrier coatings," *Surface & Coatings Technology,* **86** [1-3] 116-126 (1996).

[39]H. Chen, X. M. Zhou, and C. X. Ding, "Investigation of the thermomechanical properties of a plasma-sprayed nanostructured zirconia coating," *Journal of the European Ceramic Society,* **23** [9] 1449-1455 (2003).

[40]G. Di Girolamo, C. Blasi, L. Pilloni, and M. Schioppa, "Microstructural and thermal properties of plasma sprayed mullite coatings," *Ceramics International,* **36** [4] 1389-1395 (2010).

[41]W. B. Gong, C. K. Sha, D. Q. Sun, and W. Q. Wang, "Microstructures and thermal insulation capability of plasma-sprayed nanostructured ceria stabilized zirconia coatings," *Surface & Coatings Technology,* **201** [6] 3109-3115 (2006).

[42]K. M. Grant, S. Kramer, J. P. A. Lofvander, and C. G. Levi, "CMAS degradation of environmental barrier coatings," *Surface & Coatings Technology,* **202** [4-7] 653-657 (2007).

[43]C. Mercer, S. Faulhaber, A. G. Evans, and R. Darolia, "A delamination mechanism for thermal barrier coatings subject to calcium-magnesium-alumino-silicate (CMAS) infiltration," *Acta Materialia,* **53** [4] 1029-1039 (2005).

[44]X. Chen, R. Wang, N. Yao, A. G. Evans, J. W. Hutchinson*, et al.*, "Foreign object damage in a thermal barrier system: mechanisms and simulations," *Materials Science and Engineering a-Structural Materials Properties Microstructure and Processing,* **352** [1-2] 221-231 (2003).

[45]K. Aizu, "Possible species of ferroelastic crystals and of simultaneously ferroelectric and ferroelastic crystals," *Journal of the Physical Society of Japan,* **27** [2] 387-396 (1969).

[46]D. Baither, M. Bartsch, B. Baufeld, A. Tikhonovsky, A. Foitzik*, et al.*, "Ferroelastic and plastic deformation of t '-zirconia single crystals," *Journal of the American Ceramic Society,* **84** [8] 1755-1762 (2001).

[47]G. Behrens, G. W. Dransmann, and A. H. Heuer, "On the isothermal martensitic-transformation in 3Y-TZP," *Journal of the American Ceramic Society,* **76** [4] 1025-1030 (1993).

[48]E. P. Butler, "Transformation-toughened zirconia ceramics," *Materials Science and Technology,* **1** [6] 417-432 (1985).

[49]M. G. Cain, M. H. Lewis, M. Backshall, S. M. Bennington, and S. Hull, *Book Neutron Scattering in Materials Science* Materials Research Society, Pittsburgh, PA, 1995.

[50]C. J. Chan, F. F. Lange, M. Ruhle, J. F. Jue, and A. V. Virkar, "Ferroelastic domain switching in tetragonal zirconia single-crystals microstructural aspects," *Journal of the American Ceramic Society,* **74** [4] 807-813 (1991).

[51]A. G. Evans and R. M. Cannon, "Toughening of brittle solids by martensitic transformations," *Acta Metallurgica,* **34** [5] 761-800 (1986).

[52]A. Foitzik, M. Stadtwaldklenke, and M. Ruhle, "Ferroelasticity of the t-ZrO2," *Zeitschrift Fur Metallkunde,* **84** [6] 397-404 (1993).

[53]R. C. Garvie, R. H. Hannink, and R. T. Pascoe, "Ceramic steel," *Nature,* **258** [5537] 703-704 (1975).

[54]R. H. J. Hannink, P. M. Kelly, and B. C. Muddle, "Transformation toughening in zirconia-containing ceramics," *Journal of the American Ceramic Society,* **83** [3] 461-487 (2000).

[55]A. H. Heuer, "Transformation toughening in ZrO2-containing ceramics," *Journal of the American Ceramic Society,* **70** [10] 689-698 (1987).

[56]P. M. Kelly and L. R. F. Rose, "The martensitic transformation in ceramics - its role in transformation toughening," *Progress in Materials Science,* **47** [5] 463-557 (2002).

[57]F. F. Lange, "Transformation toughening. 5. Effect of temperature and alloy on fracture toughness," *Journal of Materials Science,* **17** [1] 255-262 (1982).

[58]F. F. Lange, "Transformation-toughened ZrO2 - Correlations between grain-size control and composition in the system ZrO2-Y2O3," *Journal of the American Ceramic Society,* **69** [3] 240-242 (1986).

[59]B. S. Li, J. S. Cherng, K. J. Bowman, and I. W. Chen, "Domain switching as a toughening mechansims in tetragonal zirconia," *Journal of the American Ceramic Society,* **71** [7] C362-C364 (1988).

[60]R. M. McMeeking and A. G. Evans, "Mechanics of transformation-toughening in brittle materials," *Journal of the American Ceramic Society,* **65** [5] 242-246 (1982).

[61]K. Mehta, J. F. Jue, and A. V. Virkar, "Grinding-induced texture in ferroelastic tetragonal zirconia," *Journal of the American Ceramic Society,* **73** [6] 1777-1779 (1990).

[62]K. Mehta and A. V. Virkar, "Fracture Mechansims in Ferroelectric-Ferroelastic Leaad Zirconate Titanate Zr-Ti=0.54-0.46 Ceramics," *Journal of the American Ceramic Society,* **73** [3] 567-574 (1990).

[63]K. M. Prettyman, J. F. Jue, A. V. Virkar, C. R. Hubbard, O. B. Cavin, *et al.*, "Hysteresity effects in 3mol percent yttria-doped zirconia (t' phase)," *Journal of Materials Science,* **27** [15] 4167-4174 (1992).

[64]P. E. Reyesmorel, J. S. Cherng, and I. W. Chen, "Transformation plasticity of CeO2-stabilized tetragonal zirconia polycrystals. 2. Pseudoelasticity and shape memory effect," *Journal of the American Ceramic Society,* **71** [8] 648-657 (1988).

[65]L. R. F. Rose, "The mechanics of transformation toughening," *Proceedings of the Royal Society of London Series a-Mathematical Physical and Engineering Sciences,* **412** [1842] 169-197 (1987).

[66]C. Q. Ru and R. C. Batra, "Toughening due to transformations induced by a crack-tip stress-field in ferroelastic materials," *International Journal of Solids and Structures,* **32** [22] 3289-3305 (1995).

[67]T. A. Schaedler, R. M. Leckie, S. Kramer, A. G. Evans, and C. G. Levi, "Toughening of nontransformable t '-YSZ by addition of titania," *Journal of the American Ceramic Society,* **90** [12] 3896-3901 (2007).

[68]G. V. Srinivasan, J. F. Jue, S. Y. Kuo, and A. V. Virkar, "Ferroelastic domain switching in polydomain tetragonal zirconia single-crystals," *Journal of the American Ceramic Society,* **72** [11] 2098-2103 (1989).

[69]A. V. Virkar and R. L. K. Matsumoto, "Ferroelastic domain switching as a toughening mechanism in tetragonal zirconia," *Journal of the American Ceramic Society,* **69** [10] C224-C226 (1986).

[70]A. H. Heuer, F. F. Lange, M. V. Swain, and A. G. Evans, "Transformation toughening - An overview," *Journal of the American Ceramic Society,* **69** [3] R1-R4 (1986).

[71]T. K. Gupta, J. H. Bechtold, R. C. Kuznicki, L. H. Cadoff, and B. R. Rossing, "Stabilization of tetragonal phase in polycrystalline zirconia," *Journal of Materials Science,* **12** [12] 2421-2426 (1977).

[72]F. R. Chien, F. J. Ubic, V. Prakash, and A. H. Heuer, "Stress-induced martensitic transformation and ferroelastic deformation adjacent microhardness indents in tetragonal zirconia single crystals," *Acta Materialia,* **46** [6] 2151-2171 (1998).

[73]J. MartinezFernandez, M. JimenezMelendo, and A. DominguezRodriguez, "Ferroelasticity of the displacive tetragonal phase in Y2O3 partially stabilized ZrO2 (Y-PSZ) single crystals," *Journal of Materials Research,* **11** [8] 1972-1978 (1996).

[74]C. Mercer, J. R. Williams, D. R. Clarke, and A. G. Evans, "On a ferroelastic mechanism governing the toughness of metastable tetragonal-prime (t ') yttria-stabilized zirconia," *Proceedings of the Royal Society a-Mathematical Physical and Engineering Sciences,* **463** [2081] 1393-1408 (2007).

[75]A. G. Evans, "Perspective on the development of high-toughness ceramics," *Journal of the American Ceramic Society,* **73** [2] 187-206 (1990).

[76]J. M. Cairney, N. R. Rebollo, M. Ruhle, and C. G. Levi, "Phase stability of thermal barrier oxides: A comparative study of Y and Yb additions," *International Journal of Materials Research,* **98** [12] 1177-1187 (2007).

[77]T. A. Schaedler, O. Fabrichnaya, and C. G. Levi, "Phase equilibria in the TiO2-YO1.5-ZrO2 system," *Journal of the European Ceramic Society,* **28** [13] 2509-2520 (2008).

[78]T. A. Schaedler, W. Francillon, A. S. Gandhi, C. P. Grey, S. Sampath, *et al.*, "Phase evolution in the YO1.5-TiO2-ZrO2 system around the pyrochlore region," *Acta Materialia,* **53** [10] 2957-2968 (2005).

[79]P. Barberis, T. MerleMejean, and P. Quintard, "On Raman spectroscopy of zirconium oxide films," *Journal of Nuclear Materials,* **246** [2-3] 232-243 (1997).

[80]D. J. Kim, H. J. Jung, and I. S. Yang, "Raman-spectroscopy of tetragonal zirconia solid solutions," *Journal of the American Ceramic Society,* **76** [8] 2106-2108 (1993).

[81]J. R. Ferraro, K. Nakamoto, and C. W. Brown, *Book Introductory Raman Spectroscopy*, Amsterdam, The Netherlands, 2003.

[82]R. Loudon, "Theory of stimulated Raman scattering from lattice vibrations," *Proceedings of the Physical Society of London,* **82** [527] 393-400 (1963).

[83]R. Loudon, "Raman effect in crystals," *Advances in Physics,* **13** [52] 423-482 (1964).

[84]D. H. Rank and J. A. Vanhorn, "Fine structures in Raman spectra," *Journal of the Optical Society of America,* **36** [8] 454-459 (1946).

[85]W. H. Weber and R. Merlin, *Book Raman Scattering in Materials Science*, Berlin, Germany, 2000.

[86]L. S. Schadler and C. Galiotis, "Fundamentals and applications of micro-Raman spectroscopy to strain-measurments in fiber-reinforced composites," *International Materials Reviews,* **40** [3] 116-134 (1995).

[87]J. G. Cai, Y. S. Raptis, and E. Anastassakis, "Stabilized cubic zirconia - A Raman-study under uniaxial stress," *Applied Physics Letters,* **62** [22] 2781-2783 (1993).

[88]R. Loudon, "Theory of first-order Raman effects in crystals," *Proceedings of the Royal Society of London Series a-Mathematical and Physical Sciences,* **275** [1360] 218-232 (1963).

[89]R. P. Bauman and S. P. S. Porto, "Lattice vibrations and structure of rare-earth fluorides," *Physical Review,* **161** [3] 842-847 (1967).

[90]D. L. Rousseau, R. P. Bauman, and S. P. S. Porto, "Normal mode determination in crystals," *Journal of Raman Spectroscopy,* **10** [JAN] 253-290 (1981).

[91]T. Merle, R. Guinebretiere, A. Mirgorodsky, and P. Quintard, "Polarized Raman spectra of tetragonal pure ZrO2 measured on epitaxial films," *Physical Review B,* **65** [14] 6 (2002).

[92]V. Milman, A. Perlov, K. Refson, S. J. Clark, J. Gavartin*, et al.*, "Structural, electronic and vibrational properties of tetragonal zirconia under pressure: a density functional theory study," *Journal of Physics-Condensed Matter,* **21** [48] 12 (2009).

[93]R. C. Garvie, "Phase analysis in zirconia systems," *Journal of the American Ceramic Society,* **55** [6] 303-305 (1972).

[94]V. Lughi and D. R. Clarke, "Temperature dependence of the yttria-stabilized zirconia Raman spectrum," *Journal of Applied Physics,* **101** [5] 6 (2007).

[95]G. J. Piermarini, S. Block, J. D. Barnett, and R. A. Forman, "Calibration of pressure-dependence of R1 ruby fluorescence line to 195 kBar," *Journal of Applied Physics,* **46** [6] 2774-2780 (1975).

[96]M. Yashima, H. Arashi, M. Kakihana, and M. Yoshimura, "Raman-scattering study of cubic-tetragonal phase-transition in Zr1-xCexO2 solid solution," *Journal of the American Ceramic Society,* **77** [4] 1067-1071 (1994).

[97]M. G. Cain, S. M. Bennington, M. H. Lewis, and S. Hull, "Study of the ferroelastic transformation in zirconia by neutron diffraction," *Philosophical Magazine B-Physics of Condensed Matter Statistical Mechanics Electronic Optical and Magnetic Properties,* **69** [3] 499-507 (1994).

[98]C. J. Howard, E. H. Kisi, R. B. Roberts, and R. J. Hill, "Neutron-diffraction studies of phase-transformations between tetragonal and orthorhombic zirconia in magnesia-partially-stabilized zirconia," *Journal of the American Ceramic Society,* **73** [10] 2828-2833 (1990).

[99]E. H. Kisi, S. J. Kennedy, and C. J. Howard, "Neutron diffraction observations of ferroelastic domain switching and tetragonal-to-monoclinic transformation in Ce-TZP," *Journal of the American Ceramic Society,* **80** [3] 621-628 (1997).

[100]Y. X. Ma, E. H. Kisi, and S. J. Kennedy, "Neutron diffraction study of ferroelasticity in a 3 mol% Y2O3-ZrO2," *Journal of the American Ceramic Society,* **84** [2] 399-405 (2001).

[101]T. M. Sabine, "Neutron-diffraction - The total powder pattern," *Australian Journal of Physics,* **33** [3] 565-572 (1980).

[102]H. H. Law, P. L. Rossiter, G. P. Simon, and J. Unsworth, "A model for the structural hysteresis in poling and thermal depoling of PZT ceramics," *Journal of Materials Science,* **30** [19] 4901-4905 (1995).

[103]S. Wan and K. J. Bowman, "Thermal depoling effects on anisotropy of lead zirconate titanate materials," *Journal of the American Ceramic Society,* **81** [10] 2717-2720 (1998).

[104]W. Chang, A. H. King, and K. J. Bowman, "Thermal effects on domain orientation of tetragonal piezoelectrics studied by in situ x-ray diffraction," *Applied Physics Letters,* **88** [24] 3 (2006).

[105]D. J. Kim, "Effect of Ta2O5, Nb2O5, and HfO2 Alloying on the Transformability of Y2O3-Stabilized Tetragonal ZrO2," *Journal of the American Ceramic Society,* **73** [1] 115-120 (1990).

VITA

Name:	Amy Marie Bolon
Address:	Department of Mechanical Engineering 3123 TAMU College Station, TX 77840-3123
Email Address:	ambolon@sbcglobal.net
Education:	B.S., Mechanical Engineering, Texas A&M University, 2009 M.S., Mechanical Engineering, Texas A&M University, 2011